

LoCuSS: Hydrostatic Mass Measurements of the High- L_X Cluster Sample – Cross-calibration of *Chandra* and *XMM-Newton*

Rossella Martino^{1,2}, Pasquale Mazzotta¹, Hervé Bourdin¹, Graham P. Smith³,
Iacopo Bartalucci¹, Daniel P. Marrone⁴, Alexis Finoguenov⁵, Nobuhiro Okabe⁶

¹Dipartimento di Fisica, Università degli Studi di Roma “Tor Vergata”, via della Ricerca Scientifica 1, 00133, Roma, Italy

²Laboratoire AIM, IRFU/Service d’Astrophysique -CEA - CNRS, Bt. 709, CEA-Saclay, 91191 Gif-sur-Yvette Cedex, France

³School of Physics and Astronomy, University of Birmingham, Birmingham, B15 2TT, England

⁴Steward Observatory, University of Arizona, 933 North Cherry Avenue, Tucson, AZ 85721, USA

⁵Department of Physics, University of Helsinki, Gustaf Hållströmin katu 2a, FI-00014 Finland

⁶Academia Sinica Institute of Astronomy and Astrophysics (ASIAA), P.O. Box 23-141, Taipei 10617, Taiwan

27 July 2018

ABSTRACT

We present a consistent analysis of *Chandra* and *XMM-Newton* observations of an approximately mass-selected sample of 50 galaxy clusters at $0.15 < z < 0.3$ – the “LoCuSS High- L_X Sample”. We apply the same analysis methods to data from both satellites, including newly developed analytic background models that predict the spatial variation of the *Chandra* and *XMM-Newton* backgrounds to $< 2\%$ and $< 5\%$ precision respectively. To verify the cross-calibration of *Chandra*- and *XMM-Newton*-based cluster mass measurements, we derive the mass profiles of the 21 clusters that have been observed with both satellites, extracting surface brightness and temperature profiles from identical regions of the respective datasets. We obtain consistent results for the gas and total hydrostatic cluster masses: the average ratio of *Chandra*- to *XMM-Newton*-based measurements of M_{gas} and M_X at r_{500} are 0.99 ± 0.02 and 1.02 ± 0.05 , respectively with an intrinsic scatter of $\sim 3\%$ for gas masses and $\sim 8\%$ for hydrostatic masses. Comparison of our hydrostatic mass measurements at r_{500} with the latest LoCuSS weak-lensing results indicate that the data are consistent with non-thermal pressure support at this radius of $\sim 7\%$. We also investigate the scaling relation between our hydrostatic cluster masses and published integrated Compton parameter Y_{sph} measurements from the Sunyaev-Zel’dovich Array. We measure a scatter in mass at fixed Y_{sph} of $\sim 16\%$ at $\Delta = 500$, which is consistent with theoretical predictions of $\sim 10 - 15\%$ scatter.

Key words: galaxies: clusters: general — X-ray:galaxies:clusters—cosmology: observations

1 INTRODUCTION

Galaxy clusters are the most massive gravitationally collapsed objects in the universe. Their abundance is determined by the spectrum of primordial density perturbations, which are amplified by gravity over the expansion history of the universe. They are therefore intricately connected to many cosmological parameters and may be used to determine precise values for them (Press & Schechter 1974; White et al. 1993; Eke et al. 1998; Allen, Schmidt & Fabian 2002; Vikhlinin et al. 2009b).

Through numerical simulations it is possible to reproduce the cluster formation mechanism, to predict the detailed shape of the mass function (Sheth & Tormen 1999; Jenkins et al. 2001; Giocoli, Tormen & van den Bosch 2008; Tinker et al. 2012) and to identify expected structural and scaling properties (e.g. Navarro, Frenk & White 1997; Kaiser 1986; Kravtsov, Vikhlinin & Nagai 2006; Springel et al. 2005). These

simulations provide the basis for the the cosmological utility of galaxy clusters, but their detailed predictions must be examined against high-quality observations in order to achieve the desired cosmological precision. Such tests can indicate the need for improved physics in the modeling, identify biases in the observational procedures (Rasia et al. 2006; Meneghetti et al. 2010; Nagai, Vikhlinin & Kravtsov 2007), and characterize the intrinsic uncertainties in the mass observables being employed. In particular, intercomparison of multiple mass estimators can provide additional checks on our understanding (e.g., Zhang et al. 2010; Mahdavi et al. 2013).

Cluster masses may be estimated from observations of the X-ray emission produced by the hot intracluster medium (ICM) within galaxy clusters. In particular, cluster mass profiles can be derived from the gas density and temperature structure, assuming the hot ICM to be in hydrostatic equilibrium within the cluster gravitational potential wells. With respect to galaxy dynamics or lensing

mass estimates, this method has the advantage of being less sensitive to projection effects due to mass along the line of sight through the cluster. However, validity of the assumptions of ICM hydrostatic equilibrium and spherical symmetry of the cluster gravitational potential wells may depend on the evolutionary state of the cluster.

The launch of the *Chandra* and *XMM-Newton* satellites has greatly improved the resolution, sensitivity, and precision of X-ray observations of galaxy clusters. Both satellites can identify clusters well beyond $z = 1$, discerning morphology and permitting temperature and mass measurements to similar distance (e.g., Maughan et al. 2008b; Semler et al. 2012; Santos et al. 2012).

However, there remain inconsistencies between measurements with the two observatories (e.g., Vikhlinin et al. 2006; Snowden et al. 2008; Nevalainen, David & Guainazzi 2010; Tsujimoto et al. 2011; Mahdavi et al. 2013). The difference between the point spread function (PSF) of the two instruments as well as different methods of background subtraction often make direct comparison difficult. The background treatment is particularly important far from cluster centers where the most cosmologically useful masses are measured. Clusters fade rapidly into the background at large radii, so the reliability of the background modeling determines the radial range over which cluster parameters can be accurately determined.

In this work, we describe X-ray data analysis technique for *Chandra* and *XMM-Newton* observations that is intended to provide consistent hydrostatic masses from either satellite at cosmologically interesting radii. Crucially, for both *Chandra* and *XMM-Newton*, we model analytically the spatial variations of all background noise components (Bartalucci et al. 2014). We apply this technique to the 50 galaxy clusters of the LoCuSS High- L_X sample (§2), estimating hydrostatic masses from all available observations from both satellites. From the sub-sample of 21 clusters observed by both, we characterize the consistency of the masses obtained from the two satellites under a consistent analysis procedure. Relationships between the X-ray masses obtained from our procedures and other cluster observables are also examined.

We describe the sample in §2. In §§3,4,5 we describe the details of the data analysis and the method of mass estimation, emphasizing the novel aspects of our technique. In §6, we examine the consistency of the mass, density, and temperature profiles between satellites. We compare our X-ray mass estimates with recent weak-lensing mass estimates to investigate observational biases. Finally, we characterize the relationship between the X-ray masses and the Sunyaev-Zel'dovich (SZ) effect signature of clusters (Y_{sz}) and quantify its scatter, comparing our results with simulations and previous works (Nagai 2006; Marrone et al. 2012; Andersson et al. 2011). We adopt a Λ CDM cosmology: $\Omega_M = 0.30$, $\Omega_\Lambda = 0.70$, $H_0 = 70 \text{ km s}^{-1} \text{ Mpc}^{-1}$.

2 SAMPLE AND OBSERVATIONS

We study a sample of 50 clusters selected from the *ROSAT* All Sky Survey catalogs (RASS; Ebeling et al. 2000; Böhringer et al. 2004). These clusters are the “High- L_X ” sample defined by the Local Cluster Substructure Survey (LoCuSS¹). The initial LoCuSS selection from the RASS catalogs applied the following criteria: $0.15 < z < 0.3$, $n_H < 7 \times 10^{20} \text{ cm}^{-2}$, $-70^\circ < \delta < 70^\circ$

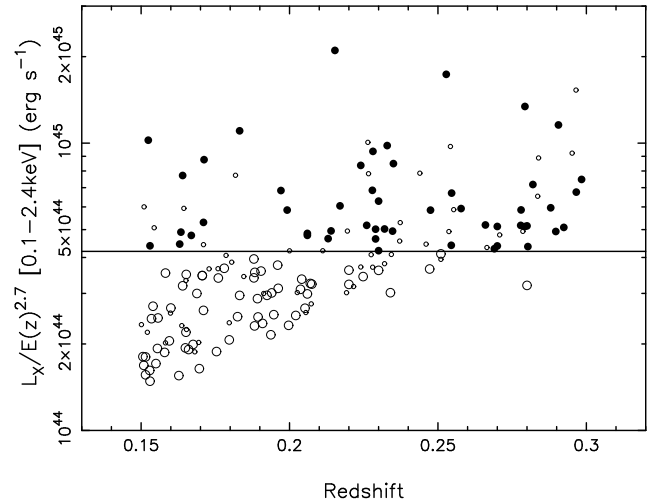


Figure 1. The LoCuSS High- L_X Sample, as defined in §2 (filled large circles). Large open circles identify clusters that satisfy the declination cut for the High- L_X sample but not the luminosity cut (horizontal line). Small open circles do not satisfy the declination cut. Clusters from the RASS parent catalogues are only plotted if they satisfy the initial selection described in §2. The absence of points from the bottom right corner of the figure is due to the RASS flux limit.

to obtain a sample of 165 clusters that span X-ray luminosities of $2 \times 10^{44} \lesssim L_X [0.1 - 2.4 \text{ keV}] \lesssim 2 \times 10^{45} \text{ erg s}^{-1}$. The 50 clusters studied in this article satisfy the following additional criteria: $-25^\circ < \delta < 65^\circ$, $L_X [0.1 - 2.4 \text{ keV}] E(z)^{-2.7} \geq 4.2 \times 10^{44} \text{ erg s}^{-1}$. The first criterion ensures that the clusters are observable at high elevation from the Subaru 8-m telescope on Mauna Kea, and the second implements an *approximate* mass selection, by adopting the Popesso et al. (2005) mass- L_X scaling relation: $L_X E(z)^{-2.7} \propto M$, where $E(z) \equiv H(z)/H_0$ is the evolution of the Hubble parameter, and ignoring scatter in the mass- L_X relation (Table 1; Figure 1). This article presents a new X-ray analysis of the entire High- L_X sample. The sub-sets of our sample of 50 clusters studied by Okabe et al. (2010), Marrone et al. (2012), and Mahdavi et al. (2012) are identified in Table 1.

All 50 clusters have been observed with either or both of *Chandra* and *XMM-Newton* (Table 1). The *Chandra* and *XMM-Newton* data are obtained with the Advanced CCD Imaging Spectrometer (ACIS) camera and the European Photon Imaging Camera (EPIC) respectively. The *Chandra* ACIS camera contains 10 planar 1024×1024 pixels CCDs: four arranged in a 2×2 array (ACIS-I), and six arranged in a 1×6 array (ACIS-S)². The *XMM-Newton* EPIC is the combination of three cameras: two MOS and a PN³.

From the full sample of 50 clusters, 43 have been observed with *Chandra*, and 39 have been observed with *XMM-Newton*. After excluding observations strongly affected by flares (§§3.1 & 3.2), useful data are available for all 50 clusters from either/both satellites. Importantly, useful data are available from *both* satellites for 27 clusters; the *Chandra* data for 21 of these 27 were obtained with ACIS-I. This relatively large sample of clusters with data from both satellites allows us to quantify the uncertainties on the hydrostatic mass measurements that are caused by instrumental cross-calibration issues. This is a main focus of our study (§6).

¹ <http://www.sr.bham.ac.uk/locuss>

² For more details see <http://cxc.cfa.harvard.edu/proposer/POG/html/chap>

³ For more details see http://xmm.esac.esa.int/external/xmm_user_support

Table 1. Cluster Sample and X-ray Observations.^aLow and high centroid shift categories are defined as $\langle w \rangle < 0.01r_{500}$ and $\langle w \rangle > 0.01r_{500}$, respectively.^bSub-samples defined thus: (1) observed with *XMM* and *Chandra* (ACIS-I VF Mode), (2) included in the Marrone et al. (2012) sample, (3) included in the Okabe et al. (2010) sample, (4) included in the Mahdavi et al. (2013) sample.^c*Chandra* ACIS-S data.^dData affected by flaring episodes for $> 90\%$ of the total exposure time; data not used for mass estimates.

Cluster	z	α, δ [J2000]	Observation IDs		Centroid shift, $\langle w \rangle / (0.01r_{500})$		Sub-samples ^{a,b}	$N_{\text{Bin,T}}$
			<i>Chandra</i>	<i>XMM-Newton</i>	<i>Chandra</i>	<i>XMM-Newton</i>		
ABELL 2697	0.232	00:03:11.98 −06:05:35.6	x	0652010401	x	0.11 ± 0.02	Low	5
ABELL 0068	0.255	00:37:06.11 +09:09:30.4	3250	0084230201	1.10 ± 0.13	1.05 ± 0.05	High	1,2,3,4 2
ABELL 2813	0.292	00:43:24.72 −20:37:24.8	9409	0042340201	1.25 ± 0.09	1.06 ± 0.04	High	1 2
ABELL 0115s	0.197	00:56:00.30 +26:20:32.5	3233	0203220101	5.52 ± 0.06	5.06 ± 0.04	High	1,3,4 3
ABELL 0141	0.230	01:05:35.82 −24:40:51.9	9410	x	4.89 ± 0.20	x	High	2
ZwCl 0104.4+0048	0.254	01:06:49.53 +01:03:22.0	10465 ^c	x	0.34 ± 0.04	x	Low	2
ABELL 0209	0.206	01:31:53.34 −13:36:44.0	3579, 522	0084230301	0.70 ± 0.10	0.62 ± 0.04	Low	1,2,3,4 2
ABELL 0267	0.230	01:52:42.32 +01:00:40.9	3580	0084230401 ^d	2.23 ± 0.05	x	High	2,3,4 2
ABELL 0291	0.196	02:01:42.99 −02:11:46.3	x	0605000301	x	0.46 ± 0.04	Low	3 6
ABELL 0383	0.188	02:48:03.38 −03:31:45.6	2320, 524	0084230501	0.17 ± 0.05	0.17 ± 0.04	Low	1,2,3,4 4
ABELL 0521	0.248	04:54:08.23 −10:14:23.6	430 ^c	0603890101	4.57 ± 0.11	5.28 ± 0.04	High	2,3,4 2
ABELL 0586	0.171	07:32:20.53 +31:37:51.8	530, 11723	0605000801 ^d	0.26 ± 0.07	x	Low	2,3,4 4
ABELL 0611	0.288	08:00:56.74 +36:03:21.6	3194 ^c	0605000601 ^d	0.33 ± 0.08	x	Low	2,3,4 2
ABELL 0697	0.282	08:42:57.71 +36:22:00.1	4217	0605000701 ^d	0.49 ± 0.08	x	Low	2,3,4 2
ZwCl 0857.9+2107	0.235	09:00:36.88 +20:53:41.5	10463 ^c	0402250701	0.18 ± 0.08	0.14 ± 0.02	Low	3
ABELL 0750	0.163	09:09:12.67 +10:58:26.6	924	0605000901 ^d	2.57 ± 0.09	x	High	3 3
ABELL 0773	0.217	09:17:52.67 +51:43:38.1	533, 3588, 5066	0084230601	1.11 ± 0.08	1.39 ± 0.04	High	1 3
ABELL 0781	0.298	09:20:24.74 +30:30:11.3	534	0150620201, 0401170101	5.43 ± 0.25	5.13 ± 0.05	High	1 2
ZwCl 0949.6+5207	0.214	09:52:49.15 +51:53:04.5	3195 ^c	x	0.33 ± 0.08	x	Low	2
ABELL 0901	0.163	09:55:57.24 −09:59:04.7	x	0148170101	x	1.03 ± 0.03	High	4
ABELL 0907	0.167	09:58:22.18 −11:03:51.6	3250, 3185, 535	0201903501, 0404910601	0.30 ± 0.04	0.35 ± 0.03	Low	1 6
ABELL 0963	0.205	10:17:03.54 +39:02:59.2	903 ^c	0084230701	0.25 ± 0.03	0.22 ± 0.02	Low	4 5
ZwCl 1021.0+0426	0.291	10:23:39.58 +04:11:10.7	9371	0108670101	0.26 ± 0.03	0.39 ± 0.02	Low	1 2
ABELL 1423	0.213	11:57:17.36 +33:36:39.4	538, 11724	x	1.27 ± 0.15	x	High	3
ABELL 1451	0.199	12:03:17.25 −21:32:14.0	x	0652010101	x	0.76 ± 0.05	Low	5
RXC J1212.3−1816	0.269	12:12:18.10 −18:18:31.4	x	0652010201	x	2.66 ± 0.12	High	3
ZwCl 1231.4+1007	0.229	12:34:21.97 +09:47:10.0	539, 11727	x	2.84 ± 0.21	x	High	2
ABELL 1682	0.226	13:06:50.97 +46:33:24.6	3244 ^d , 11725	x	2.32 ± 0.13	x	High	2
ABELL 1689	0.183	13:11:29.53 −01:20:30.3	5004, 6930, 7289	0093030101	0.17 ± 0.01	0.23 ± 0.02	Low	1,4 6
ABELL 1758	0.280	13:32:43.74 +50:32:45.0	2213 ^d	0142860201	x	1.45 ± 0.03	High	4 5
ABELL 1763	0.228	13:35:18.26 +41:00:00.7	3591	0084230901	1.15 ± 0.06	1.54 ± 0.07	Low	1,4 2
ABELL 1835	0.253	14:01:01.92 +02:52:42.8	6880, 6881, 7370	0098010101, 0147330201, 0551830101	0.23 ± 0.01	0.37 ± 0.01	Low	1,2,3,4 6
ABELL 1914	0.171	14:26:00.92 +37:49:33.2	3593	0112230201	1.49 ± 0.03	1.13 ± 0.01	High	1,3,4 3
ZwCl 1454.8+2233	0.258	14:57:15.14 +22:20:32.3	4192	0108670201	0.34 ± 0.02	0.29 ± 0.02	Low	1,2,3 7
ABELL 2009	0.153	15:00:19.50 +21:22:10.3	10438	x	0.17 ± 0.03	x	Low	4
ZwCl 1459.4+4240	0.289	15:01:20.84 +42:20:57.4	7899	0402250201	1.36 ± 0.16	1.40 ± 0.11	High	1,2,3 2
RXC J1504.1−0248	0.215	15:04:07.51 −02:48:15.2	5793	0401040101	0.12 ± 0.01	0.15 ± 0.01	Low	1 5
ABELL 2111	0.229	15:39:41.73 +34:25:04.8	11726	x	3.18 ± 0.14	x	High	4 2
ABELL 2204	0.152	16:32:46.85 +05:34:32.8	6104, 7940	0306490201, 0306490301, 0306490401	0.09 ± 0.01	0.22 ± 0.02	Low	1,4 3
ABELL 2219	0.228	16:40:21.20 +46:42:18.4	896 ^c	0605000501	1.66 ± 0.03	1.31 ± 0.04	High	2,3,4 8
RX J1720.1+2638	0.164	17:20:10.01 +26:37:30.1	4361, 3224	0500670201, 0500670301, 0500670401	0.26 ± 0.05	0.26 ± 0.02	Low	1,3 5
ABELL 2261	0.224	17:22:27.10 +32:07:56.3	5007	0093030301 ^d	0.83 ± 0.07	x	Low	2,3,4 3
RXC J2102.1−2431	0.188	21:02:09.77 −24:32:00.7	x	0652010301	x	0.34 ± 0.04	Low	5
RX J2129.6+0005	0.235	21:29:39.77 +00:05:19.1	9370, 552	0093030201	0.42 ± 0.11	0.66 ± 0.03	Low	1,2,3 2
ABELL 2390	0.232	21:53:36.89 +17:41:44.6	4193 ^c	0111270101	0.74 ± 0.03	0.64 ± 0.03	Low	2,3,4 9
ABELL 2485	0.247	22:48:30.82 −16:06:31.8	10439	x	0.50 ± 0.14	x	Low	2,3 3
ABELL 2537	0.297	23:08:22.08 −02:11:28.4	9372	0042341201, 0205330501	0.82 ± 0.11	0.65 ± 0.12	Low	1,4 2
ABELL 2552	0.300	23:11:33.23 +03:38:02.5	11730, 3288	x	0.66 ± 0.12	x	Low	2
ABELL 2631	0.271	23:37:38.70 +00:16:15.6	11728, 3248	0042341301	1.69 ± 0.14	2.77 ± 0.11	High	1,2,3 2
ABELL 2645	0.251	23:41:16.64 −09:01:23.4	11769 ^c	x	1.63 ± 0.28	x	High	2

3 X-RAY DATA ANALYSIS

The *Chandra*/ACIS-I and *XMM-Newton*/EPIC observations were analysed following a similar procedure in which we binned all events in sky coordinates and energy, using new analytical models for the background treatment. The *Chandra* ACIS-S observations, for which a particle background is not yet analytically modelled, were analyzed using a “standard technique” based on the direct subtraction of a blank field sky background event-list to the target event list. The details of these data analysis techniques are described in the following sections.

3.1 *Chandra* data preparation

To process the *Chandra* data, we use the CIAO v4.3 software, with the CALDB 4.4.3. We start from level 1 event list and we apply the charge transfer inefficiency (CTI) and time dependent gain corrections. The CTI is due to soft proton damage to the ACIS chips during the passages of the satellite through the Earth’s radiation belts and it produces a row dependence in gain, event grade, and energy resolution. (Townsend et al. 2000; Grant et al. 2005). We remove then the bad CCD pixels, taking into account hot pixels, and afterglow events caused from cosmic rays building up charge on the CCD. Furthermore, we assign RA and DEC coordinates to each detected event, applying “the aspect solution” file in which the *Chandra* dither pattern information is listed.

We then recompute the event grades, analyzing the traces left from events on detector, to distinguish the photons coming from the cluster from other particles. The grade is a number assigned to every event based on which pixels in its neighboring island are above their threshold value. The processing examines every pixel in the full CCD image and selects as events regions with bias-subtracted pixel values that both exceed the event threshold and are greater than all of the adjacent pixels (i.e., a local maximum). The surrounding neighboring pixels are then compared to the bias-subtracted split-event threshold; those that are above the threshold establish the pixel pattern. For the observations taken in FAINT telemetry mode, 3×3 islands are used. For VERY FAINT mode observations, we apply additional background screening by removing events with significantly positive pixels at the border of the 5×5 event island. On the basis of the pattern, the event is assigned a grade. With the combination of these values is possible to recognize the object events path and assign it a good ASCA grades (0, 2, 4, 6), while the other events, to which is assigned a bad ASCA grades (1, 5, and 7), are removed. Then we apply the latest gain maps available to compute calibrated photon energies.

To remove the flare episodes, we use the light curve filtering procedure described in Markevitch et al. (2003). We extract the background light curve in a CCD far from cluster in the [0.3-12] keV band for Front Illuminated chips, in the [2.5-7] keV band for S3, and in the [2.5-6] keV band for S1. We bin the light curve with $\text{binsize} = 259.28$ for FI chips and 0.3-12 keV band, or $\text{binsize} = 1037.12$ for S3 and 2.5-7 keV band, and calculate the average count rate over the standard GTI, using 3σ clipping. Then the bins above or below that mean by 20% are rejected as recommended in the Markevitch’s COOKBOOK⁴.

3.2 *XMM-Newton* data preparation

The *XMM-Newton* data are pre-processed using the *XMM-Newton*-SAS v11.0. They are then filtered through spatial and temporal wavelet analyses in order to remove the contribution of point sources and soft proton flares, following the scheme described in Bourdin & Mazzotta (2008). To detect and remove high solar flares periods, we analyze light curves with associated high energy events ([10.0-12.0] keV) and softer events ([1.0-5.0] keV). This two-step analysis first enables us to isolate the most prominent flares at high energy, where ICM brightness is expected to be negligible, and also detect some of the flares with softer spectra. For each curve, we use a “B3-spline à-trous” wavelet algorithm to remove both intervals with no data and the points exceeding a 2σ significance the light-curve fluctuation.

3.3 *Chandra* ACIS-I and *XMM-Newton* EPIC observations

Chandra ACIS-I and *XMM-Newton* EPIC observations are analyzed following a procedure described in Bourdin & Mazzotta (2008, hereafter BM08) where all event-lists are merged in sky coordinates and energy building a single energy position event cube. This event cube is first used to identify point-sources, that are masked during the analysis, adopting an object separation algorithm derived from the multi-scale vision model (Bijaoui & Rue 1995).

Following an approach detailed in BM08, we similarly binned two quantities useful for imaging and spectroscopy: the effective exposure time and the estimate of a background noise level. The effective exposure includes spatial variations of the mirror effective area and detector quantum efficiency at low energy resolution, the CCD gaps and bad pixels, and a correction for the telescope motion. These quantities are extracted from the *Chandra* Calibration data base (CALDB 4.4.3), the EPIC Current Calibration files (CCFs) and the events list. The background model array is modeled as the sum of components accounting for the Galactic foreground and the Cosmic X-ray Background, as well as false photon detections due to charged particle-induced and out-of-time events. More details about this multi-component background modeling are provided in the following.

3.3.1 *Galactic foreground and the Cosmic X-ray Background*

The Cosmic X-ray background is modeled with an absorbed power law of index $\gamma = 1.42$ (see e.g. Lumb et al. 2002), while the Galactic foregrounds are modeled by the sum of two absorbed thermal components accounting for the Galactic transabsorption emission (TAE, $kT_1 = 0.099$ keV, $kT_2 = 0.248$ keV, see Kuntz & Snowden 2000) and an unabsorbed thermal component accounting for the local hot bubble (LHB, $kT_{LHB} = 0.1$ keV, see e.g. Kuntz & Snowden 2000). Being associated with real photon detections, these components are corrected for the effective areas of each telescope. In most cases, these components are modeled in an outer annulus of the field-of-view corresponding to $r \geq r_{500}$, where the cluster emissivity itself is negligible. As for the few nearest clusters in our sample for which the cluster emissivity is not spatially separable from its background, we constrain the emissivities of each background component from a joint fit of the cluster emissivity and temperature. We check the goodness of such a multi-component fit, verifying that cluster temperatures thus measured in an outer annulus of the field-of-view are lower than the average cluster temperature, as is commonly observed in clusters allowing a full cluster-foreground

⁴ <http://cxc.harvard.edu/contrib/maxim/acisbg/COOKBOOK>

spatial separation (see e.g. Pratt et al. 2007; Leccardi & Molendi 2008).

3.3.2 Analytic particle background model for ACIS-I very faint mode

For *Chandra* ACIS-I VF particle background we use the new particle background model proposed by Bartalucci et al. (2014). Here we describe the main features of the model.

Related to the interaction of highly energetic particle with the detector, the ACIS-I instrumental background is spectrally characterised by the superposition of several fluorescence emission lines $L(E, y)$ onto a continuum $C(E, y)$:

$$F_i(E, y) = C_i(E, y) + L_i(E, y), \quad (1)$$

where E is the energy, y is the CHIPY coordinate and i is the CCD chip index with $i = [0, 1, 2, 3]$. To isolate its flux from any sky component, an analytical model of the continuum ([0.3-0.7] keV, [4-5.8] keV and [6-7] keV bands) has been fitted to stowed observations performed in the so called very faint mode, and gathered over the 8 years D+E period starting in 2001. The image in the continuum band of the stowed background shows a spatial correlation of the flux of this continuum with the chip readout direction (Bartalucci et al. 2014). To characterize the spectrum of the continuum emission, it is been extracted, for each CCD, the spectrum in four adjacent strip regions along y direction: each strip region is a rectangle with $(\Delta x, \Delta y) = (1024, 256)$ pixels. These spectra show the same shape but different normalization. The continuum, therefore, is modeled with a power law plus an exponential (position independent) multiplied by the normalization factor that accounts for the observed gradient α_i :

$$C_i(E, y) = \alpha_i(y) \left(B_1 e^{-B_2 E} + B_3 E^{-B_4} \right), \quad (2)$$

where $B_1 = 0.1493$, $B_2 = 3.8106$, $B_3 = 0.0859$, $B_4 = 0.0292$ are found fitting the equation 2 to the overall spectrum extracted from all the CCD using the continuum band.

For fidelity to the observational configuration as well as statistical purposes, the emission lines are subsequently fitted to blank sky observations of the D+E period ($t_{\text{exp}} \simeq 1.5 \times 10^6$ sec), jointly to all background components. A total of 11 emission lines are found, 6 of which being position and energy dependent. They are modeled as:

$$L_i(E, y) = D(E) + \sum_{\ell=1}^3 S_{\ell,i}(E, y) \quad (3)$$

to take into account both the contribution from pure emission lines and the effect related to the over-correction of Charge Transfer Inefficiency (CTI) which splits 3 emission lines into a mother plus a daughter line (Hickox & Markevitch 2006). In particular, L is the group of emission lines which remain constant along all the CCDs while $S_{\ell,i}(E, y)$ is the group of line which varies spatially along the chip. We normalize the background in the [9.5-10.6] keV energy band as suggested in (Bartalucci et al. 2014). This band is chosen: i) because at this energy the ACIS-I effective area is a factor of ~ 100 lower than at its peak and ii) to minimize the effect related to prediction error for the mother-daughter line system at E 9keV.

The median value of the fraction of the cleaned events in the band [0.5-2.5]keV attributed to the total background component (Galactic foreground + Cosmic X-ray Background + particle background) for our sample is of $\sim 20\%$, 50% and 80% at the three radii r_{2500} , r_{1000} and r_{500} considered in this work (see section 6).

3.3.3 Analytic particle background model for XMM-Newton EPIC

For *XMM-Newton* EPIC particle background we use the particle background model described in Bourdin et al. (2013).

The *XMM-Newton* EPIC particle background is modeled from observations performed in the Filter Wheel Closed (FWC) position during revolutions 230 to 2027 as for the EPIC-MOS cameras, and 355 to 1905 as for the EPIC-PN camera. Following an approach proposed in e.g. Kuntz & Snowden (2008) or Leccardi & Molendi (2008), this model sums a quiescent continuum to a set of fluorescence emission lines convolved with the energy response of each detector. Depending on the solar flare contamination, it is occasionally completed with residual emission associated with soft protons. To account for two different spectral shapes in the soft and hard bands, the quiescent continuum is modeled as the product of a power law with an inverted error function increasing in the soft band. We set the emission line energies to the values reported in Leccardi & Molendi (2008), while the soft proton residual is modeled using an additional power law. The EPIC-MOS quiescent continuum exhibits a small emissivity gradient along the RAWY coordinate, which has been measured and taken into account in the model. This effect is presumably due to differences in the collecting areas of the imaging and readout detector regions. The fluorescence lines exhibit a more complex spatial variation (see e.g. Lumb et al. 2002; Kuntz & Snowden 2008). We modeled the emissivity distribution of the most prominent lines⁵ from the wavelet filtering of a set of FWC event images closely straddling each line energy.

Also for *XMM-Newton* observations, the median value of the fraction of the cleaned events in the band [0.5-2.5]keV attributed to the total background component is of $\sim 20\%$, 50% and 80% at the three radii r_{2500} , r_{1000} and r_{500} (see section 6).

3.4 Chandra ACIS-S observations

The *Chandra* ACIS-S particle background is not yet analytically modeled, so we analyze ACIS-S observations by means of the direct subtraction of a blank field sky background event-list from the target event list, as described, e.g. in Vikhlinin et al. (2005). The blank field sky background is processed identically to the cluster data and reprojected onto the sky using the aspect information from the cluster pointing. We renormalize the blank field sky to the background in each observation, considering a region of the ACIS field of view free from cluster emission (mainly ACIS-S1 for ACIS-S observations) and a spectral band (9.5-12 keV) where the *Chandra* effective area is nearly zero; therefore, all the observed flux is due to the particle background. This is possible because the ACIS background above 9 keV is dominated by events from the charged particles, and its spectrum is very stable despite secular and short-term variations of up to 30% in its intensity.

In addition to the particle-induced background, we check whether the diffuse soft X-ray background could be an important factor in our observations and whether adjustments are required. For each observation, we follow the procedure of Vikhlinin et al. (2005): extracting a spectrum in the source-free regions of the detector, subtracting the renormalized blank-field background, and fitting the residuals in XSPEC (in the [0.4-2.0] keV band) with an unabsorbed MEKAL model, whose normalization was allowed to

⁵ Namely the Al, Si and Cu, Ni complexes for the EPIC-MOS and EPIC-PN cameras, respectively.

be negative. The obtained best-fit model is therefore included as an additional component in the spectral fits (with its normalization scaled by the area).

3.5 ACIS-I and XMM-Newton EPIC Imaging and Spectroscopy

For *Chandra* ACIS-I and *XMM-Newton* EPIC data, the imaging and the spectral analysis is performed as in BM08. Surface brightness profiles are computed from soft energy ([0.5–2.5keV]) photon images, corrected for background and effective area. The surface brightness profile is extracted in concentric annuli centered on the centroid of the cluster. The maximum radius is set to r_{500} , which is estimated using the r - Y_x scaling relation, if the field of view permits. The minimum radius is chosen to exclude the cool cores or internal regions with evidence of isophotal asymmetry, likely due to merger events.

Spectra are also extracted in annuli around the cluster centroid. The radial boundaries are chosen so that any annulus contains ≥ 3000 counts. For each cluster, the number of annuli of the temperature profile is listed in the Tab. 1. Each spectrum is binned in energy to have at least 20 counts per bin. We fit the spectra in the [0.7–10keV] band to an absorbed single-temperature thermal model (WABS(APEC)), where the metallicity and the temperature is allowed to be free in each annulus. In most cases the absorbing column density N_H , is fixed at the value provided by Dickey & Lockman (1990) radio surveys, but we always check that it is consistent with the observed spectrum. For each extraction region and detector, this spectral model is added to the expected background spectrum (see also sect. 3.3.1), altered by the effective exposure, multiplied by the mirror effective area and detector quantum efficiency and convolved by a redistribution function of the photon energies. This function has been computed via an averaging of the redistribution functions relative to each event position and registration date. To reduce the computation time, these latter functions have been pre-tabulated in detector coordinates and rebinned within our energy axes. More precisely, we computed them within 128 tiles of the ACIS-I CCDs, 3 regions of the EPIC-MOS and 10 regions of the EPIC-PN detectors. This was undertaken by using the *Chandra* Interactive Analysis of Observations (CIAO) software and CALDB 4.4.3, and through an energy rebinning of the canned redistribution matrixes provided in the *XMM-Newton* calibration data base.

3.6 CIAO Imaging and Spectroscopy

For ACIS-S observations, the imaging and the spectral analysis is performed using the CIAO software. Starting from the new processed event file, we build images in the [0.5–2.5keV] energy band, which maximizes the cluster to background flux ratio in *Chandra* data. We subtract the blank-field background from the cluster images and create flat-fielded images using exposure maps that include corrections for CCD gaps and vignetting. Point-like sources are removed with a detection routine based on the wavelet decomposition technique documented in Vikhlinin et al. (1998). The point sources are identified using the small scales of the wavelet decomposition and the corresponding regions are masked out from all further analysis.

We then extract the surface brightness and temperature profiles in region chosen similarly for ACIS-I (that is the camera of reference having a smaller effective area and so, usually, less total counts) and XMM-Newton data as described in §3.5. During

the spectrum extraction, the background spectrum is taken from the renormalized blank-field observations using the same region of the source. We fit the [0.7–10] keV spectra to an absorbed single-temperature thermal model (WABS(MEKAL)), where the metallicity and the temperature are allowed to be free in each annulus, and the absorbing column density N_H is fixed at the value provided by Dickey & Lockman (1990) radio survey.

4 DENSITY, 3-D TEMPERATURE AND MASS PROFILES

The surface brightness and projected temperature profiles are used to derive density and 3-D temperature profiles. This is performed using the “forward” method described in, e.g., Meneghetti et al. (2010). In particular, following Vikhlinin et al. (2005), we assume a modified β -model profile for the density distribution, to accommodate a power-law behavior in the center and the observed steepening of the surface brightness in the outskirts (e.g. Vikhlinin, Forman & Jones 1999; Neumann 2005; Ettori & Balestra 2009), with the addition of a second β -model to better reproduce the core profile:

$$n_p n_e(r) \equiv \frac{n_0^2 (r/r_c)^{-\alpha}}{[1 + (r/r_c)^2]^{3\beta-\alpha/2}} + \frac{n_{02}^2}{[1 + (r/r_{c2})^2]^{3\beta_2}}, \quad (4)$$

where α , β , β_2 , n_0 , n_{02} , r_c and r_{c2} are free parameters. These profiles are then projected along the line of sight, in cylindric shells matching the radial bins of the surface brightness profiles. For *XMM-Newton* data, this projection includes convolution with the instrument PSF. The temperature profile is modeled with a power-law with the form:

$$T_{3D}(r) = T_0 \frac{(r/r_t)^{-a}}{[1 + (r/r_t)^2]^{c/2}}. \quad (5)$$

The temperature profiles are then projected along the line of sight using the “spectroscopic-like temperature” (Mazzotta et al. 2004):

$$T_{sl} = \frac{\int W T_{3D} dV}{\int W dV} \quad (6)$$

where

$$W = \frac{n_p n_e}{T_{3D}^{3/4}}. \quad (7)$$

The best-fit parameters are determined from a χ^2 minimization technique by comparing the projected quantities derived from the models with the observations.

When the low number of counts do not allow us to have a temperature profile with more than two annuli, we assume a constant profile with $a = c = r_t = 0$ in the formula 5.

4.1 Mass derivation

The density and 3-D temperature profiles are used to estimate the total gravitating mass assuming the hydrostatic equilibrium condition (Sarazin 1988):

$$M(r) = - \frac{2.22 \times 10^{13} M_\odot}{\mu} T_{3D}(r) r \times \left(\frac{d \ln \rho_g(r)}{d \ln r} + \frac{d \ln T_{3D}(r)}{d \ln r} \right) \quad (8)$$

where μ is the mean molecular weight in a.m.u. taken to be 0.5964 and $\rho_g(r)$ is the gas density profile. The T_{3D} is in units of KeV and r in units of Mpc. The gas density is derived from the ICM

particle number density profile, given directly by the analytic fit to the projected emission measure profile. For a primordial He abundance and abundances of heavier elements $Z = 0.3Z_{\odot}$, $\rho_g(r) = 1.24\sqrt{n_p n_e(r)} * m_p$, with m_p being the proton mass.

Given $M(r)$, we can calculate the total matter density profile, $\rho_{tot} = (4\pi r^2)^{-1} dM/dr$. The total mass is derived from a complex combination of parameters used in the models of $\rho_g(r)$ and $T_{3D}(r)$, with their uncertainties estimated with the bootstrap method. The observed data are used to generate a set of random realizations, assuming a Poisson distribution for the total counts in each annulus and a gaussian distribution for the projected temperature. Each realization is then fitted by the model described in the previous sections. The best fit and the errors are the mean value and the standard deviation of the resulting fits.

Our analytic model for $T_{3D}(r)$ allows very steep gradients. In some cases, such profiles are formally consistent with the observed projected temperatures because projection produces steep gradients. However, large values of dT_{3D}/dr often lead to unphysical mass estimates, for example, the profiles with $\rho_{tot} < 0$ at some radius. We eliminated this problem in the parametric bootstrap simulations by accepting only those realizations in which the best-fit $T_{3D}(r)$ leads to $\rho_{tot} > \rho_{gas}$ in the radial range covered by the data and discarding the others.

Therefore, the strength of the forward method using the analytical functions 4 and 5 is to describe a wide range of the possible profiles. In addition, simulations (Rasia et al. 2006; Meneghetti et al. 2010) show that the resulting mass reconstruction is in agreement with the resulting mass reconstruction obtained by a non parametric-model that uses directly a global deprojection of the data. This indicates that the systematic effect coming from the assumptions of these analytical forms, is negligible for the mass estimate.

5 X-RAY MORPHOLOGY

We adopt the X-ray centroid shift as a measure of X-ray morphology (following: Forman & Jones 1982; Buote & Tsai 1995; Poole et al. 2006; Maughan et al. 2008a; Böhringer et al. 2010; Marrone et al. 2012). The centroid shift parameter $\langle w \rangle$ is defined as the standard deviation of the projected separation between the X-ray peak and the centroid of emission calculated in circular apertures centered on the X-ray peak. We measure $\langle w \rangle$ (in unit of pixels) for each cluster in our sample following the method described in Mohr et al. (1995) as implemented by Maughan et al. (2008a). The analysis is performed on exposure-corrected and source-masked images in the energy band [0.7–2.0 keV], binned to 1 arcsec² pixels for both *Chandra* and *XMM-Newton*. The circular apertures have a minimum radius equal to 30 kpc, so that the core is excised from the calculation of the centroid, and the maximum radius decreases from r_{500} to $0.05r_{500}$ in steps of 5% of r_{500} . The core is included only for the determination of the X-ray peak position. The error on $\langle w \rangle$ is derived from the standard deviation observed in cluster images resimulated with Poisson noise, following Böhringer et al. (2010). The $\langle w \rangle$ is then normalized in unit of $10^{-2}r_{500}$.

Previous observational studies of the $\langle w \rangle$ distribution and the comparison with simulations (e.g. Marrone et al. 2012; Maughan et al. 2008a; Pratt et al. 2009; Böhringer et al. 2010) have adopted a dividing line between “High- w ” and “Low- w ” sub-samples at $\langle w \rangle = 10^{-2}r_{500}$. “High- w ” clusters typically show an irregular X-ray morphology due to cluster-cluster merger activity,

while “Low- w ” clusters are characterized by a regular and more circular X-ray morphology that is generally associated with clusters being in dynamical equilibrium. However note that the interpretation of Low- w clusters may be degenerate to spherical, dynamically relaxed clusters and clusters that are merging along an axis close to the observer’s line of sight (Marrone et al. 2012). Nevertheless, we adopt this definition of Low- and High- w sub-samples to aid interpretation of our results, and comparison of them with the literature. We classify 21/50 clusters as “High- w ” and 29/50 as “Low- w ” (Table 1). Furthermore, we notice that the clusters having both *Chandra* and *XMM-Newton* data, have $\langle w \rangle$ values consistent with each other.

6 RESULTS

We extract electron density, gas mass, hydrostatic mass, and temperature profiles for all 50 clusters from the X-ray data, using the techniques from §§3 & 4. For each cluster, the gas masses and hydrostatic masses are derived within three different radii, r_{Δ} , with $\Delta = 2500, 1000$ and 500 , where r_{Δ} is the clustercentric radius containing the mass $M_{\Delta} = \Delta \bar{\rho}^4 \pi r_{\Delta}^3$, with $\bar{\rho}$ the critical density of the Universe at the redshift of the cluster (Tables 2 & 3).

We describe our main results below, beginning with a comparison of *Chandra* and *XMM-Newton* measurements of the 21 clusters that have been observed with both *Chandra*/ACIS-I and *XMM-Newton* in §6.1, moving on to a comparison of our new X-ray measurements and published weak-lensing mass measurements in §6.2, and closing with a comparison of the X-ray measurements and published measurements of the Sunyaev-Zeldovich Effect in §6.3.

6.1 Cross-calibration of *Chandra* and *XMM-Newton*

The gas density and de-projected temperature profiles from the *Chandra*/ACIS-I and *XMM-Newton* data agree within the statistical errors (Figure 2). The agreement is particularly good on the scales over which cluster mass is typically measured for cosmological studies, i.e. between r_{2500} and r_{500} – see vertical lines in Figure 2. However, the agreement may be an artefact of the large uncertainties on these scales. Moreover, despite the good agreement within the errors, the *Chandra*-based temperature profiles generally lie above the *XMM-Newton*-based profiles, e.g. ABELL 0383 (bottom row of Figure 2). We therefore compare the measurements of the de-projected temperature profiles between the two satellites and between the different detectors/cameras on-board *XMM-Newton*. The details of this rather technical exercise are presented in the Appendix; we summarize the main points in the following paragraph.

We extract 4 spectra from the same circular region within r_{500} for ACIS-I, MOS1, MOS2 and PN, excluding flux from point sources, and gaps between the detectors used in all four instruments by masking identical regions from all datasets. We consider the *Chandra* spectrum as the reference spectrum and fit it in the [0.3–10.0] keV energy band with an absorbed APEC model with temperature, metallicity and N_H as free parameters. Then, we compare the resulting best fit model with the spectra obtained from the other cameras. The average ratio of temperature measurements between the satellites is measured to be: $\langle T_{XMM}/T_{Chandra} \rangle = 0.91 \pm 0.03$, where T_{XMM} is based on all three cameras, PN, MOS1, and MOS2. However this disagreement between satellites masks the differences between the three *XMM-Newton* cameras, with MOS1 reporting temperatures 4% higher than the *XMM-Newton* mean and 8% higher than PN (Table A2). We conclude that, based on their current

Table 2. Hydrostatic mass measurements

Cluster	Radii (Mpc)			<i>Chandra</i> Masses ($10^{14} M_{\odot}$)			<i>XMM-Newton</i> Masses ($10^{14} M_{\odot}$)		
	r_{2500}	r_{1000}	r_{500}	M_{2500}	M_{1000}	M_{500}	M_{2500}	M_{1000}	M_{500}
ABELL 2697	0.51	0.84	1.20	x	x	x	2.43 ± 0.15	4.38 ± 0.38	6.29 ± 0.65
ABELL 0068	0.58	0.97	1.40	3.85 ± 1.57	7.22 ± 2.79	10.77 ± 4.10	3.22 ± 0.25	6.69 ± 0.53	10.44 ± 0.86
ABELL 2813	0.50	0.86	1.24	2.54 ± 0.60	4.99 ± 1.13	7.64 ± 1.71	2.04 ± 0.25	4.07 ± 0.46	6.32 ± 0.69
ABELL 0115s	0.35	0.61	0.89	0.81 ± 0.30	1.63 ± 0.47	2.54 ± 0.73	0.49 ± 0.08	1.63 ± 0.14	3.26 ± 0.21
ABELL 0141	0.34	0.67	1.02	0.81 ± 0.51	2.33 ± 0.96	3.97 ± 1.37	x	x	x
ZwCl 0104.4+0048	0.34	0.54	0.76	0.71 ± 0.03	1.16 ± 0.05	1.67 ± 0.07	x	x	x
ABELL 0209	0.48	0.80	1.15	1.96 ± 0.38	3.64 ± 0.70	5.47 ± 1.07	1.72 ± 0.07	3.45 ± 0.12	5.45 ± 0.18
ABELL 0267	0.51	0.82	1.17	2.48 ± 0.80	4.15 ± 1.29	5.97 ± 1.84	x	x	x
ABELL 0291	0.38	0.65	0.94	x	x	x	0.99 ± 0.11	1.91 ± 0.33	2.92 ± 0.56
ABELL 0383	0.48	0.75	1.01	2.01 ± 0.48	2.95 ± 0.74	3.68 ± 0.90	1.62 ± 0.09	2.48 ± 0.22	3.25 ± 0.45
ABELL 0521	0.27	0.77	1.23	1.70 ± 0.43	4.21 ± 0.93	6.78 ± 1.48	0.34 ± 0.02	3.44 ± 0.17	7.05 ± 0.34
ABELL 0586	0.49	0.78	1.08	2.08 ± 0.32	3.27 ± 0.63	4.42 ± 0.90	x	x	x
ABELL 0611	0.51	0.84	1.20	2.68 ± 0.45	4.66 ± 0.75	6.80 ± 1.08	x	x	x
ABELL 0697	0.60	1.03	1.50	4.21 ± 1.07	8.53 ± 1.86	13.14 ± 2.74	x	x	x
ZwCl 0857.9+2107	0.42	0.66	0.91	1.89 ± 1.49	3.65 ± 2.81	5.59 ± 3.99	1.19 ± 0.11	1.81 ± 0.18	2.33 ± 0.23
ABELL 0750	0.47	0.72	0.96	1.81 ± 0.51	2.61 ± 0.95	3.17 ± 1.22	x	x	x
ABELL 0773	0.56	0.88	1.21	3.23 ± 0.55	4.92 ± 0.94	6.51 ± 1.62	3.00 ± 0.27	5.48 ± 0.59	7.77 ± 0.94
ABELL 0781	0.31	0.73	1.13	0.77 ± 0.67	3.27 ± 1.78	6.09 ± 2.87	0.61 ± 0.04	3.45 ± 0.22	6.72 ± 0.45
ZwCl 0949.6+5207	0.41	0.66	0.93	1.24 ± 0.08	2.03 ± 0.14	2.90 ± 0.20	x	x	x
ABELL 0901	0.37	0.58	0.79	x	x	x	0.83 ± 0.10	1.32 ± 0.22	1.68 ± 0.39
ABELL 0907	0.51	0.80	1.08	2.33 ± 0.38	3.50 ± 0.59	4.36 ± 0.74	2.05 ± 0.12	3.65 ± 0.37	5.17 ± 0.64
ABELL 0963	0.55	0.85	1.14	2.68 ± 0.45	4.66 ± 0.75	6.80 ± 1.08	2.41 ± 0.14	4.05 ± 0.40	5.60 ± 0.71
ZwCl 1021.0+0426	0.55	0.89	1.26	3.27 ± 0.41	5.44 ± 0.67	7.83 ± 0.96	2.89 ± 0.06	4.76 ± 0.10	6.82 ± 0.14
ABELL 1423	0.54	0.85	1.18	2.99 ± 1.05	4.50 ± 1.06	6.02 ± 1.53	x	x	x
ABELL 1451	0.50	0.92	1.36	x	x	x	2.30 ± 0.66	5.51 ± 0.89	8.97 ± 2.18
RXC J1212.3–1816	0.36	0.57	0.76	x	x	x	0.93 ± 0.21	1.42 ± 0.26	1.67 ± 0.31
ZwCl 1231.4+100	0.21	0.76	1.23	0.19 ± 0.12	3.22 ± 0.80	6.82 ± 1.29	x	x	x
ABELL 1682	0.47	0.84	1.24	2.06 ± 0.98	4.64 ± 2.00	7.35 ± 3.06	x	x	x
ABELL 1689	0.71	1.11	1.51	6.22 ± 0.52	9.51 ± 0.93	12.09 ± 1.54	5.50 ± 0.40	9.01 ± 0.96	11.98 ± 1.94
ABELL 1758	0.39	0.88	1.38	x	x	x	1.11 ± 0.19	5.23 ± 0.60	10.21 ± 1.54
ABELL 1763	0.50	0.89	1.33	2.38 ± 0.63	5.28 ± 1.27	8.61 ± 1.96	1.92 ± 0.15	4.10 ± 0.34	6.60 ± 0.56
ABELL 1835	0.68	1.11	1.57	5.81 ± 0.53	10.14 ± 1.56	14.52 ± 2.90	4.78 ± 0.18	9.24 ± 0.60	14.04 ± 1.27
ABELL 1914	0.68	1.03	1.38	5.37 ± 0.92	7.48 ± 1.21	9.11 ± 1.59	4.59 ± 0.59	6.59 ± 0.90	8.08 ± 1.00
ZwCl 1454.8+2233	0.46	0.75	1.06	1.89 ± 0.36	3.28 ± 0.91	4.61 ± 1.33	1.58 ± 0.07	2.60 ± 0.22	3.65 ± 0.42
ABELL 2009	0.55	0.91	1.28	2.87 ± 0.58	5.08 ± 1.33	7.33 ± 2.47	x	x	x
ZwCl 1459.4+4240	0.44	0.73	1.08	1.89 ± 1.49	3.65 ± 2.81	5.59 ± 3.99	1.68 ± 0.10	3.54 ± 0.22	5.65 ± 0.36
RXC J1504.1–0248	0.61	1.01	1.47	4.16 ± 1.28	7.95 ± 3.60	13.15 ± 7.11	3.65 ± 0.15	7.10 ± 0.42	10.93 ± 0.82
ABELL 2111	0.47	0.80	1.17	2.01 ± 0.70	3.94 ± 1.27	5.99 ± 1.89	x	x	x
ABELL 2204	0.71	1.10	1.49	6.14 ± 0.90	9.08 ± 1.45	11.16 ± 1.75	4.90 ± 0.39	8.02 ± 0.81	10.66 ± 1.72
ABELL 2219	0.71	1.20	1.75	2.68 ± 0.45	4.66 ± 0.75	6.80 ± 1.08	4.25 ± 0.31	8.80 ± 0.97	14.35 ± 2.04
RX J1720.1+2638	0.56	0.88	1.23	3.06 ± 0.38	4.71 ± 0.81	6.38 ± 1.72	2.77 ± 0.10	4.79 ± 0.33	6.97 ± 0.68
ABELL 2261	0.58	0.90	1.22	3.66 ± 1.00	5.46 ± 1.52	6.75 ± 1.89	x	x	x
RXC J2102.1–2431	0.43	0.70	1.00	x	x	x	1.35 ± 0.13	2.36 ± 0.34	3.52 ± 0.61
RX J2129.6+0005	0.48	0.76	1.08	1.98 ± 0.25	3.25 ± 0.39	4.65 ± 0.56	1.81 ± 0.07	2.95 ± 0.11	4.22 ± 0.16
ABELL 2390	0.64	1.10	1.59	2.68 ± 0.45	4.66 ± 0.75	6.80 ± 1.08	4.10 ± 0.30	8.80 ± 0.92	13.67 ± 2.09
ABELL 2485	0.46	0.78	1.11	1.80 ± 0.43	3.58 ± 1.16	5.32 ± 2.08	x	x	x
ABELL 2537	0.51	0.83	1.18	2.73 ± 0.74	4.60 ± 1.21	6.65 ± 1.73	2.51 ± 0.23	4.73 ± 0.45	7.20 ± 0.73
ABELL 2552	0.53	0.88	1.25	3.04 ± 0.70	5.34 ± 1.14	7.81 ± 1.64	x	x	x
ABELL 2631	0.44	0.82	1.20	1.70 ± 0.43	4.21 ± 0.93	6.78 ± 1.48	1.96 ± 0.25	5.12 ± 0.60	8.51 ± 0.98
ABELL 2645	0.47	0.80	1.15	2.23 ± 1.08	4.05 ± 1.80	5.98 ± 2.59	x	x	x

Table 3. Gas mass measurements

Cluster	<i>Chandra</i> Gas Masses ($10^{14} M_{\odot}$)			<i>XMM-Newton</i> Gas Masses ($10^{14} M_{\odot}$)		
	$M_{\text{gas},2500}$	$M_{\text{gas},1000}$	$M_{\text{gas},500}$	$M_{\text{gas},2500}$	$M_{\text{gas},1000}$	$M_{\text{gas},500}$
ABELL 2697	x	x	x	0.275 ± 0.009	0.567 ± 0.022	0.880 ± 0.037
ABELL 0068	0.322 ± 0.078	0.619 ± 0.111	0.903 ± 0.135	0.316 ± 0.001	0.633 ± 0.004	0.928 ± 0.008
ABELL 2813	0.300 ± 0.041	0.642 ± 0.069	1.014 ± 0.092	0.290 ± 0.005	0.625 ± 0.006	0.999 ± 0.007
ABELL 0115s	0.091 ± 0.024	0.270 ± 0.049	0.546 ± 0.089	0.086 ± 0.000	0.264 ± 0.001	0.519 ± 0.003
ABELL 0141	0.083 ± 0.036	0.295 ± 0.064	0.550 ± 0.084	x	x	x
ZwCl 0104.4+0048	0.236 ± 0.004	0.161 ± 0.003	0.236 ± 0.004	x	x	x
ABELL 0209	0.244 ± 0.028	0.564 ± 0.059	0.972 ± 0.094	0.226 ± 0.001	0.531 ± 0.002	0.909 ± 0.003
ABELL 0267	0.232 ± 0.038	0.449 ± 0.064	0.703 ± 0.094	x	x	x
ABELL 0291	x	x	x	0.123 ± 0.006	0.245 ± 0.018	0.391 ± 0.031
ABELL 0383	0.180 ± 0.018	0.302 ± 0.026	0.425 ± 0.036	0.175 ± 0.001	0.300 ± 0.001	0.433 ± 0.002
ABELL 0521	0.230 ± 0.039	0.626 ± 0.068	1.027 ± 0.088	0.053 ± 0.000	0.579 ± 0.001	1.198 ± 0.003
ABELL 0586	0.221 ± 0.016	0.402 ± 0.033	0.600 ± 0.049	x	x	x
ABELL 0611	0.612 ± 0.039	0.406 ± 0.028	0.612 ± 0.039	x	x	x
ABELL 0697	0.423 ± 0.059	0.936 ± 0.095	1.485 ± 0.127	x	x	x
ZwCl 0857.9+2107	0.190 ± 0.076	0.412 ± 0.151	0.675 ± 0.187	0.154 ± 0.001	0.263 ± 0.002	0.382 ± 0.004
ABELL 0750	0.154 ± 0.020	0.277 ± 0.041	0.406 ± 0.061	x	x	x
ABELL 0773	0.317 ± 0.030	0.599 ± 0.056	0.907 ± 0.102	0.307 ± 0.001	0.589 ± 0.002	0.869 ± 0.003
ABELL 0781	0.084 ± 0.060	0.420 ± 0.121	0.783 ± 0.142	0.076 ± 0.001	0.422 ± 0.001	0.771 ± 0.004
ZwCl 0949.6+5207	0.315 ± 0.010	0.200 ± 0.007	0.315 ± 0.010	x	x	x
ABELL 0901	x	x	x	0.074 ± 0.004	0.137 ± 0.010	0.208 ± 0.020
ABELL 0907	0.235 ± 0.018	0.425 ± 0.030	0.623 ± 0.042	0.246 ± 0.001	0.443 ± 0.002	0.648 ± 0.004
ABELL 0963	0.612 ± 0.039	0.406 ± 0.028	0.612 ± 0.039	0.279 ± 0.001	0.500 ± 0.003	0.714 ± 0.003
ZwCl 1021.0+0426	0.422 ± 0.024	0.739 ± 0.036	1.082 ± 0.048	0.473 ± 0.001	0.800 ± 0.001	1.151 ± 0.002
ABELL 1423	0.216 ± 0.043	0.435 ± 0.056	0.711 ± 0.095	x	x	x
ABELL 1451	x	x	x	0.235 ± 0.044	0.627 ± 0.051	1.046 ± 0.102
RXC J1212.3–1816	x	x	x	0.069 ± 0.009	0.138 ± 0.010	0.196 ± 0.012
ZwCl 1231.4+100	0.018 ± 0.011	0.374 ± 0.060	0.828 ± 0.078	x	x	x
ABELL 1682	0.180 ± 0.057	0.460 ± 0.103	0.764 ± 0.137	x	x	x
ABELL 1689	0.570 ± 0.021	0.944 ± 0.036	1.285 ± 0.059	0.573 ± 0.002	0.946 ± 0.004	1.250 ± 0.007
ABELL 1758	x	x	x	0.154 ± 0.021	0.716 ± 0.041	1.218 ± 0.062
ABELL 1763	0.274 ± 0.046	0.705 ± 0.093	1.229 ± 0.135	0.265 ± 0.001	0.688 ± 0.003	1.233 ± 0.005
ABELL 1835	0.606 ± 0.025	1.076 ± 0.065	1.554 ± 0.120	0.643 ± 0.002	1.138 ± 0.003	1.615 ± 0.007
ABELL 1914	0.521 ± 0.038	0.844 ± 0.054	1.163 ± 0.073	0.503 ± 0.001	0.823 ± 0.003	1.141 ± 0.004
ZwCl 1454.8+2233	0.222 ± 0.017	0.392 ± 0.040	0.578 ± 0.060	0.223 ± 0.000	0.403 ± 0.001	0.608 ± 0.002
ABELL 2009	0.261 ± 0.024	0.481 ± 0.049	0.708 ± 0.082	x	x	x
ZwCl 1459.4+4240	0.190 ± 0.076	0.412 ± 0.151	0.675 ± 0.187	0.180 ± 0.001	0.415 ± 0.002	0.684 ± 0.003
RXC J1504.1–0248	0.485 ± 0.066	0.858 ± 0.179	1.301 ± 0.337	0.525 ± 0.001	0.928 ± 0.002	1.347 ± 0.004
ABELL 2111	0.181 ± 0.040	0.427 ± 0.074	0.719 ± 0.110	x	x	x
ABELL 2204	0.529 ± 0.036	0.905 ± 0.062	1.279 ± 0.082	0.588 ± 0.003	1.004 ± 0.002	1.385 ± 0.008
ABELL 2219	0.612 ± 0.039	0.406 ± 0.028	0.612 ± 0.039	0.690 ± 0.003	1.448 ± 0.010	2.324 ± 0.023
RX J1720.1+2638	0.296 ± 0.017	0.521 ± 0.038	0.771 ± 0.083	0.306 ± 0.001	0.550 ± 0.001	0.821 ± 0.003
ABELL 2261	0.383 ± 0.050	0.688 ± 0.088	1.004 ± 0.127	x	x	x
RXC J2102.1–2431	x	x	x	0.146 ± 0.006	0.280 ± 0.017	0.450 ± 0.033
RX J2129.6+0005	0.249 ± 0.015	0.475 ± 0.025	0.749 ± 0.037	0.254 ± 0.000	0.476 ± 0.001	0.744 ± 0.002
ABELL 2390	0.612 ± 0.039	0.406 ± 0.028	0.612 ± 0.039	0.583 ± 0.003	1.225 ± 0.007	1.861 ± 0.023
ABELL 2485	0.163 ± 0.020	0.354 ± 0.051	0.558 ± 0.087	x	x	x
ABELL 2537	0.242 ± 0.033	0.470 ± 0.056	0.739 ± 0.081	0.242 ± 0.002	0.475 ± 0.004	0.725 ± 0.009
ABELL 2552	0.316 ± 0.037	0.644 ± 0.064	1.022 ± 0.094	x	x	x
ABELL 2631	0.230 ± 0.039	0.626 ± 0.068	1.027 ± 0.088	0.223 ± 0.002	0.601 ± 0.005	0.970 ± 0.008
ABELL 2645	0.541 ± 0.117	0.328 ± 0.079	0.541 ± 0.117	x	x	x

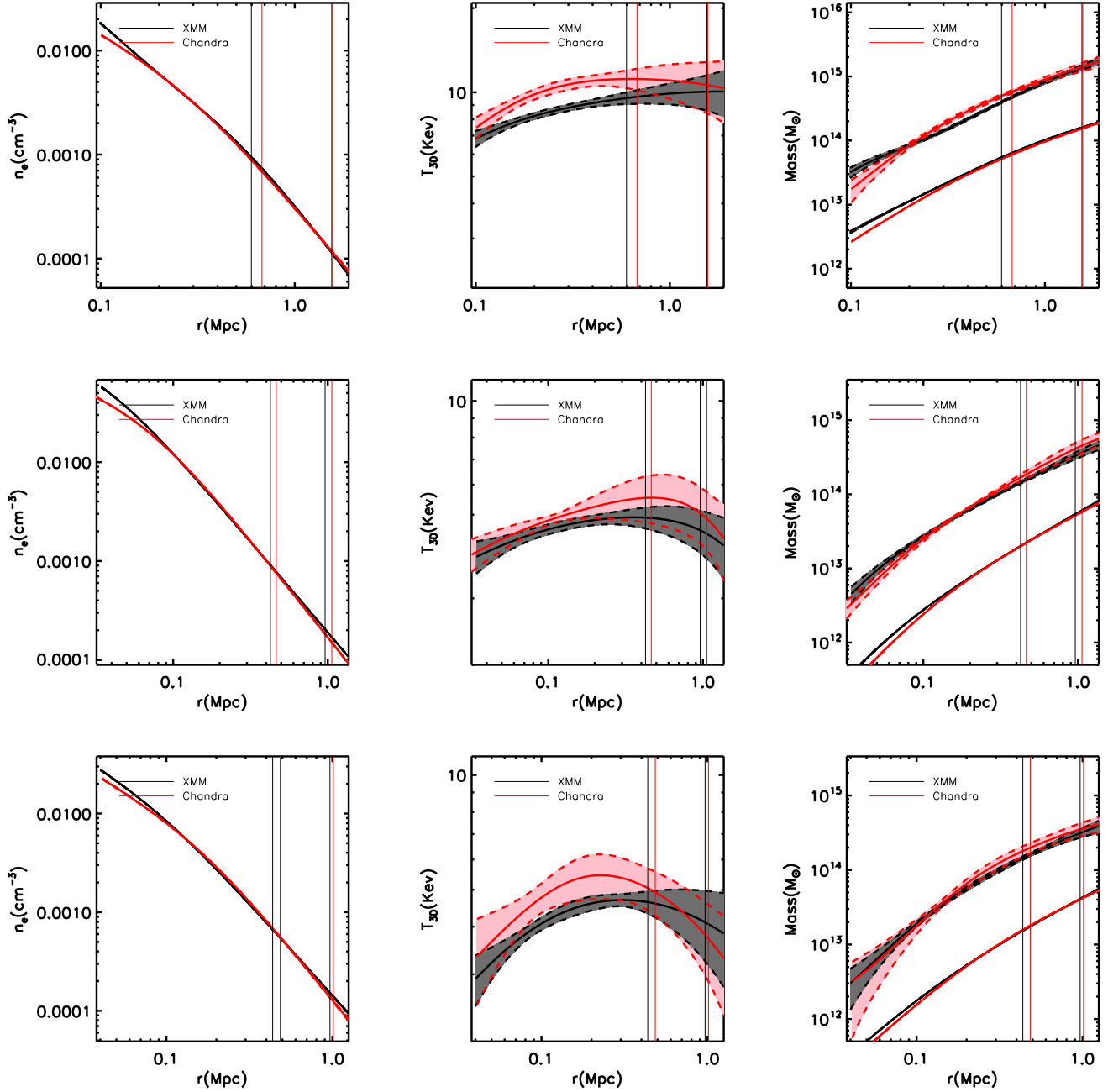


Figure 2. Gas density (left), de-projected temperature (centre) and gas mass and total hydrostatic mass profiles (right), for three representative clusters from the High- L_X sample: ABELL01835 (top row), ZwCl 1454.8+2233 (middle row), and ABELL0383 (bottom row). The vertical lines indicate r_{2500} and r_{500} , respectively. *Chandra* is plotted in red; *XMM-Newton* in black. The shaded regions and dashed curves delineate the respective 1σ uncertainties.

calibration files, X-ray temperature measurements currently suffer $\sim 4 - 9\%$ systematic uncertainty between satellites and between cameras. The temperature differences between satellites and instruments seems to depend on cluster temperature, based on fitting a two-parameter model to the respective measurements, T_1 and T_2 : $T_1 = AT_2^\alpha$. We obtain best fits of $\alpha = 0.81 \pm 0.17$, 0.92 ± 0.17 , 0.83 ± 0.14 , 0.84 ± 0.12 and $A = 1.24 \pm 0.31$, 2.50 ± 0.42 , 1.29 ± 0.39 , 1.24 ± 0.31 for the PN/ACIS-I, MOS1/ACIS-I, MOS2/ACIS-I and ALL 3 XMM CAMERAS/ACIS-I combina-

tions respectively. In each case a larger discrepancy is found at higher temperatures.

Chandra and *XMM-Newton* gas mass measurements agree with each other within the uncertainties (Figure 3 & Table 4), based on fitting the model to the data: $M_{CXO}/M_0 = a_\Delta (M_{XMM}/M_0)^\alpha$, and minimizing a modified error-weighted χ^2 statistic (Mahdavi et al. 2008; Press et al. 1992). In Table 4 we report the measured parameter values with two different treatments of the slope (α), both as a free parameter of the fit, and with α fixed to 1. This agreement holds well at all three over-density considered:

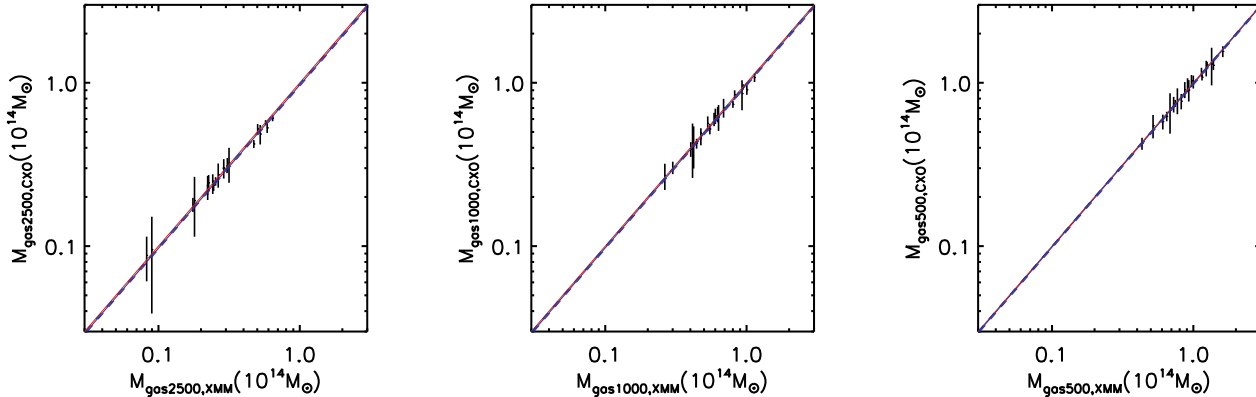


Figure 3. *Left panel:* *Chandra* gas mass versus *XMM-Newton* gas mass at r_{2500} : the solid blue line is the best fit relation with fixed slope = 1; the dashed blue lines are the errors of the best fit at 1σ , the solid red line is the expected line 1:1. *Middle panel:* *Chandra* gas mass versus *XMM-Newton* gas mass at r_{1000} , similarly for *Chandra* versus *XMM-Newton* gas mass at r_{2500} . *Right panel:* *Chandra* gas masses versus *XMM-Newton* gas mass at r_{500} , with lines similar for r_{2500} and r_{1000} .

$\Delta = 500, 1000, 2500$. We therefore conclude that the satellites measure the same X-ray flux within the $[0.5\text{--}2.5\text{keV}]$ energy band to 2% precision.

We find good agreement between the total hydrostatic mass measurements, albeit with slightly larger uncertainties (Figure 4 & Table 5). The agreement is particularly good at r_{500} , with $a_{500} = 1.02 \pm 0.05$ for the fixed-slope model, and deteriorates slightly towards higher over-densities. Despite the uncertainties on the global temperature, the agreement of the total mass is due to the agreement of the temperature profiles at larger radii. In fact, many clusters show a discrepancy of the *XMM-Newton* and *Chandra* temperature profiles in the inner part, while they are perfectly in agreement within the errors at larger radii (see Figure 2). The apparent 2σ disagreement at r_{2500} may be caused by the smearing effect of the *XMM-Newton* PSF on the temperature profile. This could modify the temperature profile of clusters with strong temperature gradients, for example cool core clusters. Note that we do not take account of the PSF when de-projecting the *XMM-Newton* temperature profile. We therefore divide the clusters into cool core and non-cool core sub-samples. Clusters are classed as cool-core if the temperature within $r < 0.15r_{500}$ is cooler than temperature within $(0.15r_{500} < r < 0.3r_{500})$ at $> 2\sigma$ significance. We obtain mean mass ratios at r_{2500} of $a_{2500} = 1.15 \pm 0.05$ and 1.13 ± 0.07 respectively. This suggests that the PSF is not the main cause of the discrepancy at $\Delta = 2500$.

Furthermore, for each cluster, we extract the spectra in two annuli with a width equal to $[0.15\text{--}0.55]r_{500}$ (Bin1) and $[0.55\text{--}1.0]r_{500}$ (Bin2), defining for our subsample two regions close to r_{2500} and r_{500} , respectively. Our purpose is to investigate if, in each bin, there is any systematics in the temperature estimate due to the number of source counts (SC_{cxo} , $Bini$ and SC_{xmm} , $Bini$) or to the fraction of background events in the spectra ($BgfC_{cxo}$, $Bini$, $BgfC_{xmm}$, $Bini$). In Figure 5, in the upper panel, we plot the *Chandra* temperature versus the *XMM-Newton* temperature in the inner bin $[0.15\text{--}0.55]r_{500}$ (left panel) and in the outer bin $[0.55\text{--}1.0]r_{500}$ (right panel). The clusters are colour-coded according to the ratio between the *Chandra* and *XMM-Newton* net counts. The red line is the relation 1:1. As expected, in the inner bin, we find that the *Chandra* temperature are in mean higher than the *XMM-Newton* ones and that the disagreement is worse going to higher

temperature. However, we can notice that the most of the estimated temperatures are higher than 6 keV, that is, as already observed in other works (Kuntz & Snowden 2008; Mahdavi et al. 2013) a *thresholding* value to make the difference between *Chandra* and *XMM-Newton* significant. In the outer bin (right panel), instead, we can notice that the most of the estimated temperatures are ≤ 6 keV. Furthermore, larger errors bars are associated to highest temperature, due to the larger difficulty to distinguish the hottest spectra having a flatter shape from the background. For this reason, these clusters have a *lower weight* in the fit of the statistical sample. However, as suggested by the colour distribution indicating the ratio between the *Chandra* and *XMM-Newton*, the net counts number affects the error bars in the outer bin but there is not evident correlation of it with the global temperature (in both bins). In the bottom panel of Figure 5 we plot the same quantities of the upper panel except for the color now indicating the ratio between the *Chandra* and *XMM-Newton* background fraction. The typical background fraction is 0.18 ± 0.04 and 0.11 ± 0.03 in the inner bin and 0.75 ± 0.16 and 0.67 ± 0.03 in the outer bin for *Chandra* and *XMM-Newton* respectively. We can notice that also in this case, there is no correlation between the temperature estimated in each bin and the number of counts attributed to the background.

We also explore mass dependence of, and intrinsic scatter in, the relationship between *Chandra*- and *XMM-Newton*-based masses, fitting a two parameter model: $M_{Cxo} = a M_{XMM}^\alpha$ to the data using the Bayesian method described by Kelly (2007). The slope parameter α is consistent with unity at all three over-densities for both gas masses and hydrostatic masses (Table 5). The intrinsic scatter is estimated to be $\sim 3\%$ for gas masses and $\sim 6 - 8\%$ for hydrostatic masses.

6.2 X-ray/weak-lensing mass comparison

We now compare our hydrostatic mass measurements with published LoCuSS weak-lensing mass measurements (Okabe et al. 2010, 2013). Okabe et al. (2013) presented a stacked weak-lensing analysis of all 50 clusters in the High- L_X sample, showing that systematic errors are sub-dominant to statistical errors. This was achieved in part via a conservative selection of background galaxies redder than the cluster red sequence. The low number density

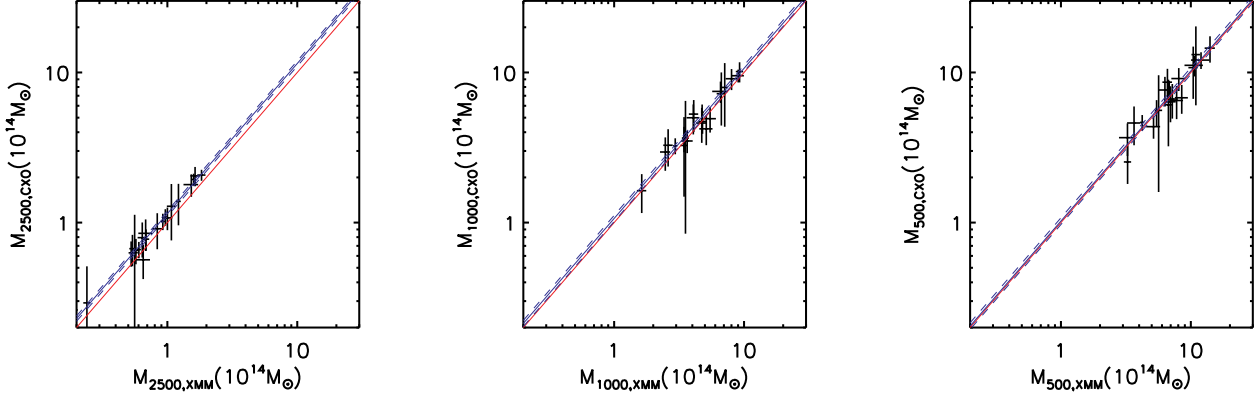


Figure 4. Left panel: *Chandra* mass versus *XMM-Newton* mass at r_{2500} : the solid blue line is the best fit relation with fixed slope = 1; the dashed blue lines are the errors of the best fit at 1σ , the solid red line is the expected line 1:1. Middle panel: *Chandra* mass versus *XMM-Newton* mass at r_{1000} , similarly for *Chandra* versus *XMM-Newton* mass at r_{2500} . Right panel: *Chandra* mass versus *XMM-Newton* mass at r_{500} , with lines similar for r_{2500} and r_{1000} .

Table 4. Comparison of gas mass measurements $M_{\text{CXO}}/M_0 = a_{\Delta} (M_{\text{XMM}}/M_0)^{\alpha}$

Δ	M_0 M_{\odot}	Fixed-slope Model a_{Δ}	Two parameters Model a_{Δ}	α
2500	3×10^{13}	0.97 ± 0.02	0.99 ± 0.02	0.95 ± 0.05
1000	6×10^{13}	0.98 ± 0.02	0.98 ± 0.02	0.96 ± 0.06
500	9×10^{13}	0.99 ± 0.02	0.99 ± 0.02	0.98 ± 0.06

Table 5. Comparison of hydrostatic mass measurements $M_{\text{CXO}}/M_0 = a_{\Delta} (M_{\text{XMM}}/M_0)^{\alpha}$

Δ	M_0 M_{\odot}	Fixed-slope Model a_{Δ}	Two parameters Model a_{Δ}	α
2500	3×10^{13}	1.15 ± 0.05	1.15 ± 0.05	1.01 ± 0.10
1000	5×10^{13}	1.06 ± 0.05	1.08 ± 0.06	0.99 ± 0.12
500	7×10^{13}	1.02 ± 0.05	1.04 ± 0.06	1.01 ± 0.15

of background galaxies therefore precluded analysis of individual clusters. Stacked weak-lensing analysis of the clusters in common between Okabe et al. (2010) and Okabe et al. (2013) revealed that on average the M_{500} measurements from the latter exceed those from the former by 20%. In anticipation of a more careful analysis based on individual cluster measurement, we therefore compare our new hydrostatic mass measurements with weak-lensing masses from Okabe et al. (2010), applying a 20% increase to the latter. This comparison is applied to the clusters in sub-sample 3 (Table 1).

We use hydrostatic masses from *Chandra*, where available, and from *XMM-Newton* otherwise. All hydrostatic masses are calculated at the over-density radii derived from the 2010 weak-lensing analysis. We follow the same approach as in the previous section to measure the mean mass ratio: $M_X = a_{\Delta} M_{\text{WL}}$. Our hydrostatic masses exceed the weak-lensing masses of Okabe et al. (2010) by $\sim 10 - 15\%$ at all over-densities with no obvious trend with over-density and dynamical state. Specifically, at r_{500} we find: $M_X / M_{\text{WL}} = 1.12 \pm 0.10$. Therefore apply-

ing the 20% increase to the Okabe et al. (2010) weak-lensing masses discussed above suggests that at r_{500} our X-ray and weak-lensing data are consistent with $M_X / M_{\text{WL}} \simeq 0.93$. This is in qualitative agreement with the theoretical expectation that $M_X < M_{\text{WL}}$, and is consistent with recent observational and theoretical studies (Nagai, Vikhlinin & Kravtsov 2007; Mahdavi et al. 2008; Zhang et al. 2010; Mahdavi et al. 2013).

A more detailed comparison is possible between our hydrostatic mass measurements and the weak lensing mass of Mahdavi et al. (2013). There are 21 clusters in common between our samples (sub-sample 4 in Table 1). Using Mahdavi et al.’s weak lensing mass and computing our hydrostatic mass measurements within their values of r_{500} , we obtain $M_X / M_{\text{WL}} = 1.07 \pm 0.06$ at $\Delta = 500$ for these 21 clusters. To achieve a careful like-for-like comparison, we repeat this calculation using Mahdavi et al.’s hydrostatic and weak-lensing measurements for the same sub-sample of 21 clusters, obtaining $M_X / M_{\text{WL}} = 0.94 \pm 0.07$, which slightly exceeds the value of $M_X / M_{\text{WL}} = 0.88 \pm 0.05$ that they obtain for their full sample. Our hydrostatic mass measurements at $\Delta = 500$ therefore exceed Mahdavi et al.’s measurements by $\sim 14\%$. Interestingly, this excess matches the difference between Mahdavi et al.’s *XMM-Newton*- and *Chandra*-based mass measurements at $\Delta = 2500$. They derived an energy-dependent correction to the *Chandra* effective area based on their cross-calibration at $\Delta = 2500$, which acts to reduce their *Chandra*-based mass measurements. This correction also reduces their *Chandra* mass measurements at $\Delta = 500$ (priv. comm. A. Mahdavi). We also find that the satellites disagree at $\Delta = 2500$ (§6.1), however we achieve close agreement between them at $\Delta = 500$, without invoking any correction to the *Chandra* effective area. We suggest that the difference between our respective hydrostatic mass measurements at $\Delta = 500$ can be in part explained by these differences between our analyses. We also note that our hydrostatic mass measurements imply that Mahdavi et al.’s weak-lensing masses may be biased low.

6.3 Scaling relation between hydrostatic mass and integrated Y parameter

We compare our X-ray hydrostatic masses and the SZ signal, $Y_{\text{sph}} D_A^2$, measured with the SZA, an 8-element radio interferom-

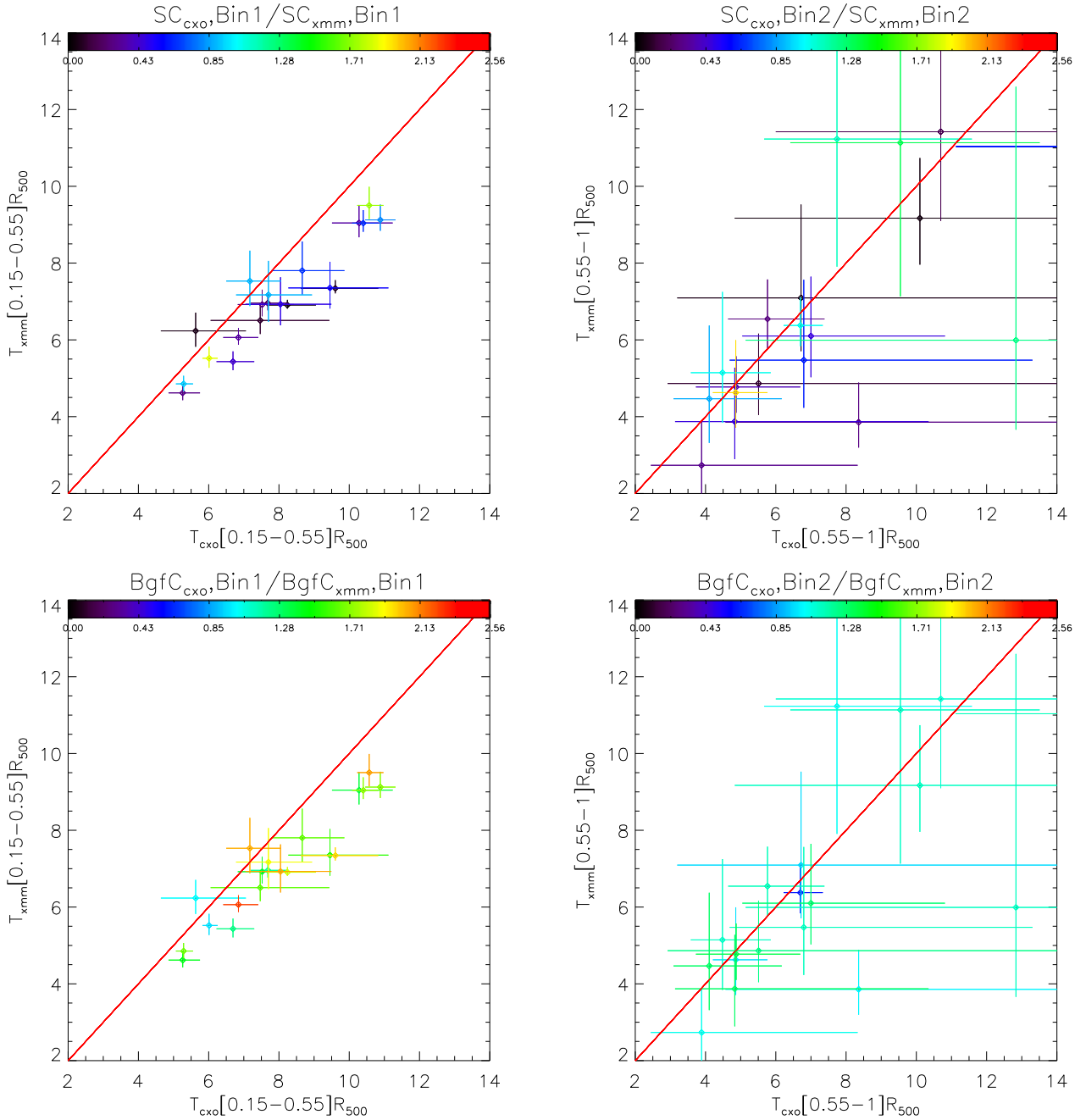


Figure 5. Upper panel: *Chandra* temperature versus the *XMM-Newton* temperature in the inner bin $[0.15-0.55]r_{500}$ (left panel) and in the outer bin $[0.15-0.55]r_{500}$ (right panel). The clusters are colour-coded according to the ratio between the *Chandra* and *XMM-Newton* net counts. The red line is the relation 1:1. Bottom panel: as upper panel but with the color indicating the ratio between the *Chandra* and *XMM-Newton* background fraction.

eter optimized for measurements of the SZ effect (Marrone et al. 2012), for the 17 clusters in sub-sample 2 (Table 1). Following Marrone et al., we fit the following model to the data:

$$\frac{M_X(r_\Delta)}{10^{14} M_\odot} = 10^A \left(\frac{Y_{\text{sph}} D_A^2 E(z)^{-2/3}}{10^{-5} \text{Mpc}^2} \right)^B, \quad (9)$$

performing the regression in linearized coordinates using the base-10 logarithm of the data points, and using the Bayesian regression method described by Kelly (2007). We perform the fits twice at each over-density, once with both A , B , and the intrinsic scatter as

free parameters, and once with the slope parameter B fixed at the self-similar value of $B = 3/5$.

Our best-fit slopes and normalizations of the fits are consistent within 68% confidence intervals with the $M_{\text{WL}} - Y_{\text{sph}}$ relation of Marrone et al. (Table 6). The fit with a free slope parameter is also consistent with the self-similar slope. Formally, the data are consistent with zero intrinsic scatter in mass at fixed Y_{sph} around the best-fit scaling relation (Table 6). However, despite the large uncertainties in our measurement of the intrinsic scatter, we note that the scatter of $\sim 15 - 20\%$ is similar to that obtained in other stud-

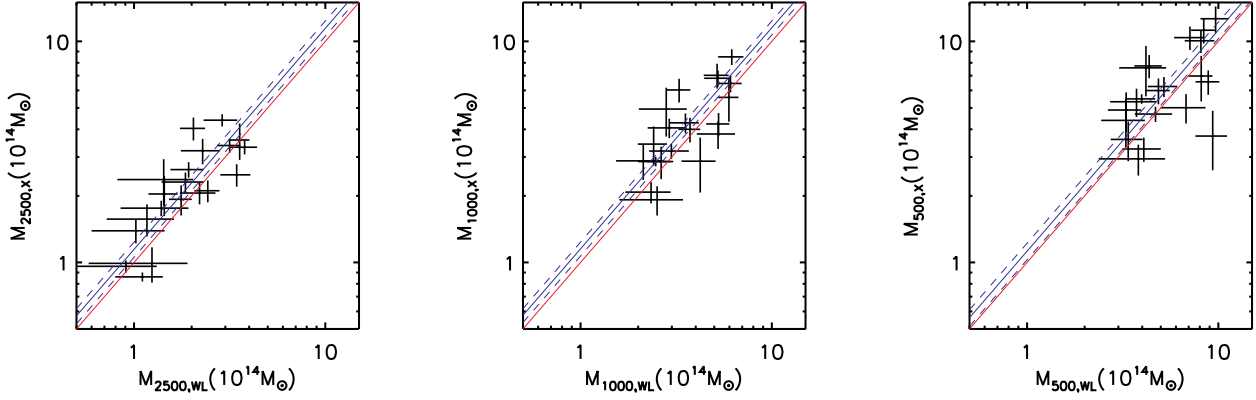


Figure 6. *Left panel:* X-ray mass versus weak lensing mass at r_{2500} : the solid blue line is the best fit relation with fixed slope = 1; the dashed blue lines are the errors of the best fit at 1σ , the solid red line is the expected line 1:1. *Middle panel:* X-ray mass versus weak lensing mass at r_{1000} , similarly for X-ray versus weak lensing mass at r_{2500} . *Bottom panel:* X-ray mass versus weak lensing mass at r_{500} , with lines similar for r_{2500} and r_{1000} .

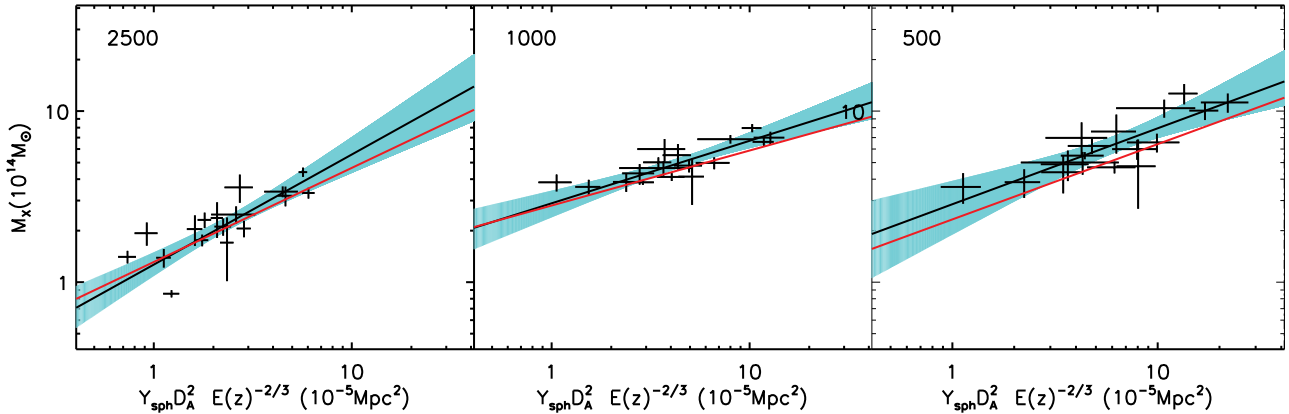


Figure 7. Our best-fit $M_{X,\Delta} - Y_{\text{sph}} D_A^2$ relations (blue line with cyan error envelope) at $\Delta = 2500$ (left), 1000 (middle) and 500 (right), plus the best-fit $M_{\text{WL}} - Y_{\text{sph}}$ relations from (Marrone et al. 2012, red).

ies (e.g. Nagai 2006; Marrone et al. 2012), and appears to decrease toward larger radii.

At $\Delta = 500$ (Fig 8), our results agree with Andersson et al. (yellow line 2011), who estimated cluster mass using the observed $M_{X,500} - Y_X$ scaling relation (Vikhlinin et al. 2009a). Furthermore, in the same figure, we compare our best-fit $M_{X,500} - Y_{\text{sph}} D_A^2$ relation with the observed $M_{X,500} - Y_{\text{sph}} D_A^2$ relation obtained by (green line Planck Collaboration 2011) using Y_{sph} measured by the *Planck* satellite and mass $M_{X,500}$ estimated from the $M_{500} - Y_{X,500}$ relation given in Arnaud et al. (2010). However we can notice in our relation that the cluster ABELL0383 affects the slope far more than any other. As discussed also in other works (Marrone et al. 2012; Planck Collaboration 2012), this cluster shows unusually low SZ flux for its apparent mass in their SZA observations. In fact, even if ABELL0383 seems to be a very relaxed system in X-rays, Zitrin et al. (2012) find that it is a cluster-lens system, having at least two other well-defined optical structures within $15'$.

Furthermore, the $M_X - Y_X$ relation obtained by

Vikhlinin et al. (2009a) (magenta line in Fig 8) is consistent with our $M_X - Y_{\text{sph}}$ relation, after re-normalising Y_X by the factor $C_{X\text{SZ}}$ following Planck Collaboration (2012). This is consistent with the ratio between Y_{sph} and $C_{X\text{SZ}} Y_X$ being close to unity, in agreement with Planck Collaboration (2012), who obtained $Y_{\text{sph}} / (C_{X\text{SZ}} Y_X) = 0.95 \pm 0.04$. We will investigate the $Y_{\text{sph}} - (C_{X\text{SZ}} Y_X)$ relationship for our full sample in a future paper.

7 DISCUSSION

A primary goal of comparing hydrostatic mass measurements from X-ray observations to weak-lensing mass measurements is to test the assumption that the cluster gas is in hydrostatic equilibrium. Predictions derived from cosmological numerical simulations indicate that the most prominent departures from hydrostatic equilibrium occur at large radius, $r \gtrsim r_{500}$, where bulk motion of gas provides additional, non-

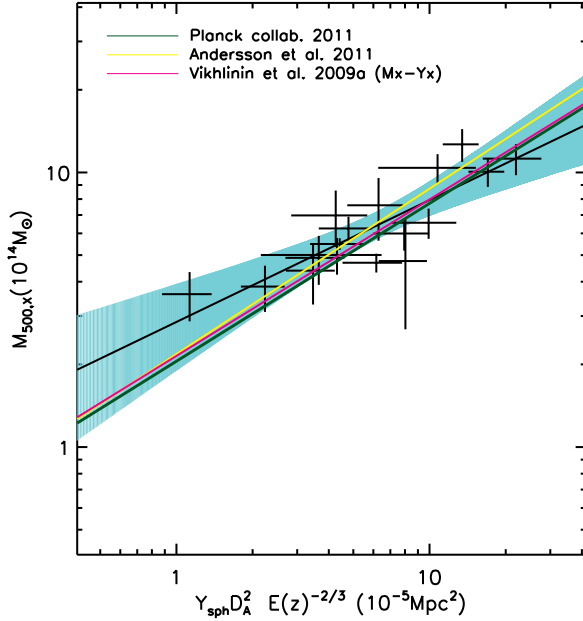


Figure 8. Our best-fit $M_{X,\Delta} - Y_{sph} D_A^2$ relations (blue line with cyan error envelope) at $\Delta = 500$, plus the best-fit relations from (Planck Collaboration 2011, green) and (Andersson et al. 2011, yellow). In magenta is plotted the best-fit $M_X - Y_X$ relation from Vikhlinin et al. (2009a)

Table 6. $M_X - Y_{sph}$ scaling relation

Δ	A	B	$\sigma_{M Y}$
2500	0.101 ± 0.070	0.649 ± 0.153	$0.225^{+0.111}_{-0.083}$
1000	0.273 ± 0.114	0.547 ± 0.159	$0.153^{+0.116}_{-0.071}$
500	0.454 ± 0.154	0.446 ± 0.182	$0.157^{+0.127}_{-0.073}$
2500	0.117 ± 0.038	3/5	$0.215^{+0.109}_{-0.120}$
1000	0.213 ± 0.041	3/5	$0.136^{+0.106}_{-0.065}$
500	0.303 ± 0.054	3/5	$0.149^{+0.121}_{-0.069}$

thermal pressure support, biasing the hydrostatic masses low (e.g. Lau, Kravtsov & Nagai 2009; Battaglia et al. 2010; Rasia et al. 2006; Nagai, Vikhlinin & Kravtsov 2007; Meneghetti et al. 2010).

In observationally establishing the magnitude of this bias, the systematic errors in the mass measurements must be accounted for. X-ray mass measurements may be systematically biased by uncertainties in instrumental calibration (Nevalainen, David & Guainazzi 2010; Tsujimoto et al. 2011), and differences in analysis methods (e.g. Mantz & Allen 2011). It can be difficult to disentangle these two effects, with up to $\sim 45\%$ differences between mass measurements based on independent observations and analysis of the same clusters reported in some cases (Rozo et al. 2012). Applications of a single analysis method to both *Chandra* and *XMM-Newton* data tend to report smaller systematic differences in mass measurements, for example, Mahdavi et al. (2013) recently reported a 15% systematic excess of *Chandra*-

based M_{500} measurements over *XMM*-based measurements of the same.

Applying a consistent method to identical cluster regions for both satellites, we find *Chandra* and *XMM-Newton* hydrostatic mass measurements that agree very well. In particular, at r_{500} we obtain $M_{CXO}/M_{XMM} = 1.01 \pm 0.05$. This agreement is achieved by combining the latest instrumental calibration with our new analysis method, incorporating an analytic model of the X-ray background. Our hydrostatic mass measurements are also consistent with a $\sim 10\%$ non-thermal pressure support at r_{500} , based on a comparison between our measurements and weak-lensing mass estimates of individual clusters from Okabe et al. (2010) and from the stacked analysis of Okabe et al. (2013). We will investigate non-thermal pressure support in more detail in a future article.

8 CONCLUSION

Accurate measurements of galaxy cluster masses are required to constrain adequately the cosmological parameters as one of several complementary probes. In this paper, we present the total hydrostatic mass and gas profiles for the 50 clusters in the approximately mass-selected LoCuSS High- L_X sample, using all the available *Chandra* and *XMM-Newton* observations. These measurements are performed using exactly the same procedure and also using two newly developed analytic background models, one for *Chandra* ACIS-I and one for *XMM-Newton*, that model the spatial variation of the background with an accuracy better than 2% and than 5%, respectively. We use this sample to investigate the cross-calibration of cluster mass measurements between *Chandra* and *XMM-Newton*. We also compare our X-ray mass with weak lensing mass estimates and integrated Compton effect Y_{SZ} measurements, investigating their observational relations and comparing with numerical simulation predictions. The main results are summarized below.

(i) For a subsample of 21 clusters, having both *Chandra* ACIS-I and *XMM-Newton* data, we derived the mass profiles extracting the surface brightness and the temperature profiles exactly in the same sky regions. This allowed us to measure the cross calibration uncertainties among the two instruments. We find that, for each cluster, the gas and total mass profiles are fully consistent within 1σ . In particular, the average ratios between the *Chandra* and *XMM-Newton* gas mass, $M_{gas,CXO}/M_{gas,XMM}$, are 0.98 ± 0.02 and 0.99 ± 0.02 at r_{1000} , and r_{500} , respectively. Agreement between the total hydrostatic masses improves to larger radii, with excellent agreement at r_{500} : $M_{CXO}/M_{XMM} = 1.02 \pm 0.05$. We find no evidence of the mass ratio being a function of mass, and just $\sim 7\%$ intrinsic scatter.

(ii) For a subsample of 22 clusters, we compare hydrostatic masses with published weak-lensing mass estimates from Okabe et al. (2010, 2013). We find that the X-ray and weak-lensing mass measurements Okabe et al. (2013) are consistent with non-thermal pressure support of $\sim 7\%$ at r_{500} . Whilst this is consistent with other recent studies, we caution that further careful analysis of individual cluster mass measurements from our weak-lensing observations are required before firm conclusions can be drawn.

(iii) For a subsample of 17 clusters, we investigate the scaling relation between our X-ray hydrostatic masses and integrated Compton parameter Y_{sph} obtained with the Sunyaev-Zel'dovich Array presented by Marrone et al. (2012). We find that the $M_X - Y_{sph}$ scaling relations, measured at $\Delta = 2500, 1000$ and 500 , have, on average, a normalization higher than Marrone et al. (2012), but consistent within the errors. Furthermore, we find a slope that is better reproduced by self similar models. Our results are also

consistent at r_{500} with Andersson et al. (2011) and Arnaud et al. (2010).

(iv) For the $M_X - Y_{sph}$ scaling relations, we find an intrinsic scatter of $\sim 15 - 22\%$, with the smaller scatter seen at larger radii. These values are slightly lower, but statistically consistent with Marrone et al., who obtained an intrinsic scatter of $\sim 20\%$ at all radii. At larger radii, our estimate of intrinsic scatter is also consistent with the $10 - 15\%$ predicted in numerical simulations (e.g. Nagai 2006).

In summary, we have presented an important step forward in our ability to measure the hydrostatic mass of galaxy clusters free from instrument- and background-related systematic errors. In the future we will compare our hydrostatic mass estimates with weak lensing masses and integrated Compton parameter measurements for the full High- L_X LoCuSS sample. This comparison, based on our *full sample*, will allow us to investigate robustly the shape, normalization and scatter of key cosmological scaling relations at low redshift.

ACKNOWLEDGMENTS

We acknowledge financial contribution from contracts ASI-INAF I/009/10/0, ASI-INAF I/088/06/0, PRIN-INAF-2009 grant “Weighing Galaxy Clusters With Strong and Weak Lensing”. PM acknowledges financial support by grants GO2-13153X and AR2-13012X issued by the Chandra X-ray Observatory Center. GPS acknowledges support from the Royal Society. We thank the anonymous referee for his/her thorough review and highly appreciate the comments and suggestions, which significantly contributed to improving the quality of the publication. We thank Arif Babul and Gabriel Pratt for comments on the draft manuscript and Andisheh Mahdavi for helpful discussions. We also acknowledge Y.-Y. Zhang, the PI of ten XMM-Newton observations that were used in our study.

APPENDIX A: EFFECTS OF INSTRUMENTAL CROSS CALIBRATION ON TEMPERATURE ESTIMATES

In §6.1, we show the existence of a good agreement between the gas mass derived with *Chandra* and *XMM-Newton* observations. This indicates that, on average, the flux measured by *Chandra* and *XMM-Newton* in the $[0.5-2.5]$ keV band is consistent. Nevertheless, the *Chandra* temperatures tend to be, on average, higher than the *XMM-Newton* ones, indicating that there are still some cross calibration problems between the two instruments. Using the overlapping *Chandra-XMM-Newton* sub-sample we quantify the total effect on the temperature based on current calibration files. This allow us to provide a lower limit for the systematic uncertainties that affect the hydrostatic mass measurements with *Chandra* and *XMM-Newton*, based on the current calibration files. To do this, for each cluster in the subsample, we extract 4 spectra from the same circular region with $r = r_{500}$ for ACIS-I, MOS1, MOS2 and PN. In extracting the spectra, we take care to exclude the common region which corresponds to the brightest point sources present in the field of view plus the combination of all the gaps of the four detectors. To highlight possible calibration problems, we consider the *Chandra* spectrum, which for convenience we use as reference spectrum for the comparison, and fit it in the $[0.3-10.0]$ keV energy band with an absorbed APEC model with temperature, metallicity and N_H as free parameters. Then, we compare the resulting best

fit model with the spectra obtained by the other cameras, using the same normalization factor. We identify three different cases that we show in the three panels of Figure A1. In the first case, shown in the top panel of the Figure A1, we find that the best fit model obtained by ACIS-I camera reproduces very well the spectra of all the other *XMM-Newton* cameras within a confidence level better than 2σ . It is worth noticing that this case seems to hold for most of the clusters in our sample.

In the second case, shown in the middle panel in Figure A1, we find that the best fit model obtained by ACIS-I camera reproduces well the spectra of some of the cameras of *XMM-Newton* but not all. In the third case, shown in the bottom panel in Figure A1, we find that the best fit model obtained by ACIS-I camera does not reproduce any of the spectra from the cameras of *XMM-Newton*. We find a disagreement between the *Chandra* spectrum and each of the three *XMM-Newton* spectra at energy lower than 0.7 KeV, which may be related to some bias in the modelling of the *Chandra* response. Such low energy discrepancies do not affect our overall analysis, which is performed in the $[0.7-10.]$ KeV energy band. Furthermore, the EPIC-PN spectra exhibit an excess at high energy with respect to the ACIS-I and EPIC-MOS spectra. This could partly be due to the presence of non-standard emission lines related to solar flare contamination that are not predicted in the particle background model. The EPIC-PN data has not been used for spectroscopic measurements in the few systems of this kind in our sample.

To quantify the average effect of the above calibration issues on the temperature measurements, we fit in the energy band $[0.7-10]$ KeV an absorbed APEC model to the spectra extracted from each single camera (ACIS-I, MOS1, MOS2 and PN) and for the combination of the three cameras of *XMM-Newton* (Table A1). In Figure A2 we compare the temperatures from the three cameras of *XMM-Newton* with the one from *Chandra*. For convenience in red we overplot the 1:1 relation. We notice that, due to the relatively large errors, if we compare the temperatures of each cluster, those are consistent within the errors at 1σ . Nevertheless, if we consider the sample, we immediately notice that, on average, *Chandra* returns higher temperatures than *XMM-Newton*. In particular, using the method described in §6.1, we derived the ratio of T_{XMM}/T_{CXO} for the different cameras as reported in table A2. We notice that the average discrepancy is of the order of $9 \pm 3\%$.

For completeness, we repeat the same analysis using only the cameras of *XMM-Newton*. This comparison is shown in Figure A3 and the results of the fit are reported in table A2. It is important to say that we find that even *XMM-Newton* alone shows significant average temperature discrepancy for some cameras. In particular, we notice that $T_{pn}/T_{M1} = 0.92 \pm 0.3$.

Finally, we investigate the possibility of a systematic trend with cluster temperature by fitting a two-parameter model to the respective temperature measurements: $T_1 = A T_2^\alpha$, where T_1 and T_2 are the temperatures obtained from different satellites/cameras, the exponent α characterizes the temperature dependence of any bias. We obtain best fits of $\alpha = 0.81 \pm 0.18, 0.92 \pm 0.18, 0.83 \pm 0.14$ for the PN/ACIS-I, MOS1/ACIS-I, MOS2/ACIS-I combinations respectively, indicating that the differences between satellites and instruments depend on cluster temperature.

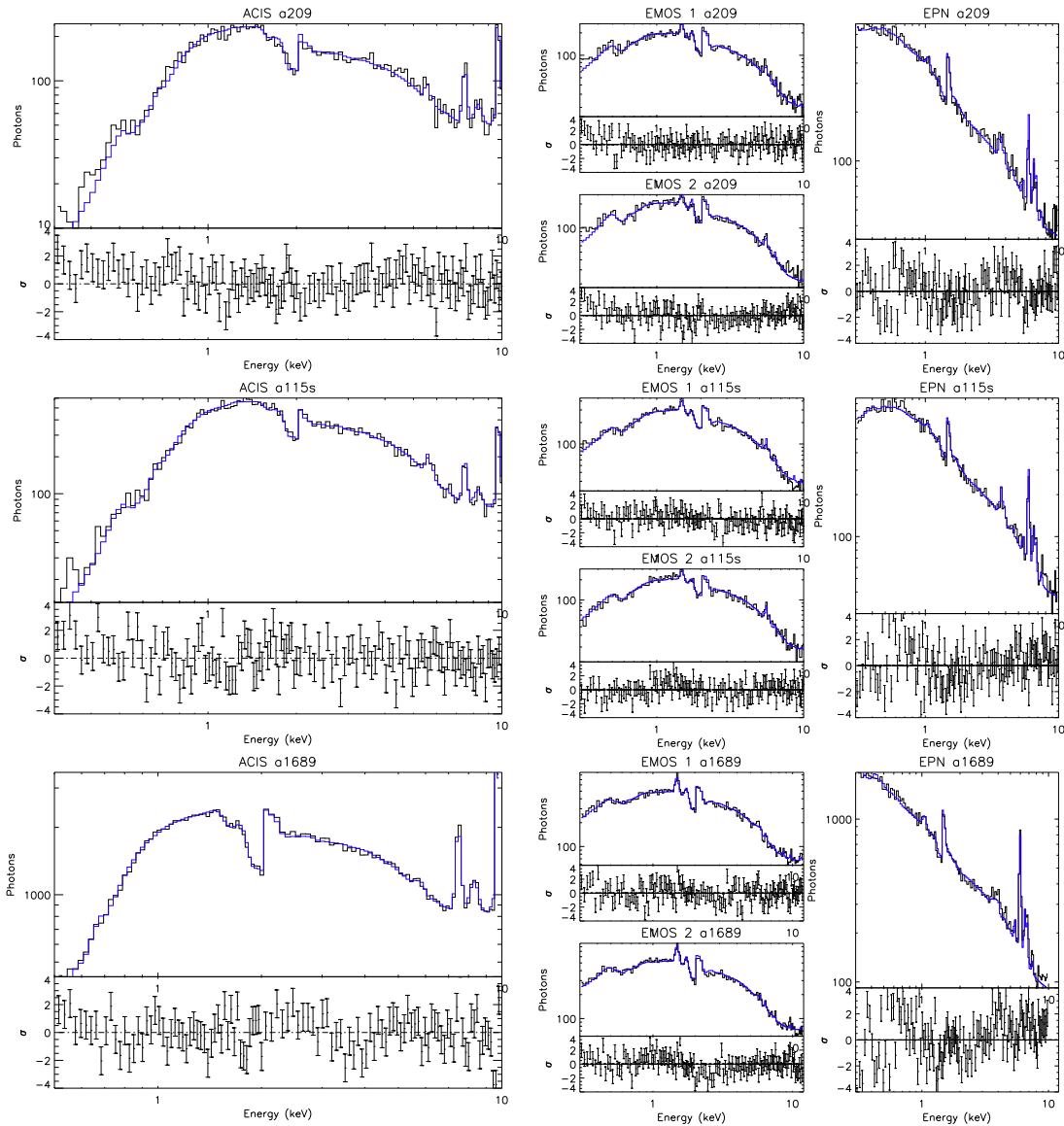


Figure A1. *Top panel:* Spectra for the cluster a209 obtained by *Chandra* ACIS-I and each of the *XMM-Newton* cameras (MOS1, MOS2 and EPN). The *Chandra* ACIS-I spectrum is fitted with an APEC model (blue line): the same model is overplotted on the spectra of the other *XMM-Newton* cameras. Residuals are plotted in the lower portion of each panel. Notice the good agreement between the data and the model for all four cameras within a 2σ average confidence interval. *Middle panel:* Same as top panel but for a115. The *Chandra* best fit model agrees well with MOS1 and MOS2 within 2σ but not with PN. *Bottom panel:* Same as top panel but for a1689. The *Chandra* ACIS-I best fit model does not reproduce any of the spectra from the *XMM-Newton* cameras, with differences beyond 4σ . Furthermore, the spectra from the three *XMM-Newton* cameras show significant differences among themselves.

REFERENCES

- Allen S., Schmidt R., Fabian A., 2002, MNRAS, 334, L11
 Andersson K. et al., 2011, ApJ, 738, 48
 Arnaud M., Pratt G. W., Piffaretti R., Böhringer H., Croston J. H., Pointecouteau E., 2010, A&A, 517, A92
 Bartalucci I., Mazzotta P., Bourdin H., Vikhlinin A., 2014, A&A, 566, A25
 Battaglia N., Bond J. R., Pfrommer C., Sievers J. L., Sijacki D., 2010, ApJ, 725, 91
 Bijaoui A., Rue, 1995, Signal Processing
 Böhringer H. et al., 2010, A&A, 514, A32+
 Böhringer H. et al., 2004, A&A, 425, 367
 Bourdin H., Mazzotta P., 2008, AAP, 479, 307
 Bourdin H., Mazzotta P., Markevitch M., Giacintucci S., Brunetti G., 2013, ApJ, 764, 82
 Buote D. A., Tsai J. C., 1995, ApJ, 452, 522
 Dickey J. M., Lockman F. J., 1990, ARA&A, 28, 215
 Ebeling H., Edge A. C., Allen S. W., Crawford C. S., Fabian A. C., Huchra J. P., 2000, MNRAS, 318, 333
 Eke V. R., Cole S., Frenk C. S., Patrick Henry J., 1998, MNRAS, 298, 1145
 Ettori S., Balestra I., 2009, A&A, 496, 343
 Forman W., Jones C., 1982, ARA&A, 20, 547
 Giocoli C., Tormen G., van den Bosch F. C., 2008, MNRAS, 386, 2135
 Grant C. E., Bautz M. W., Kissel S. M., LaMarr B., Prigozhin G. Y., 2005, in Society of Photo-Optical Instrumentation Engi-

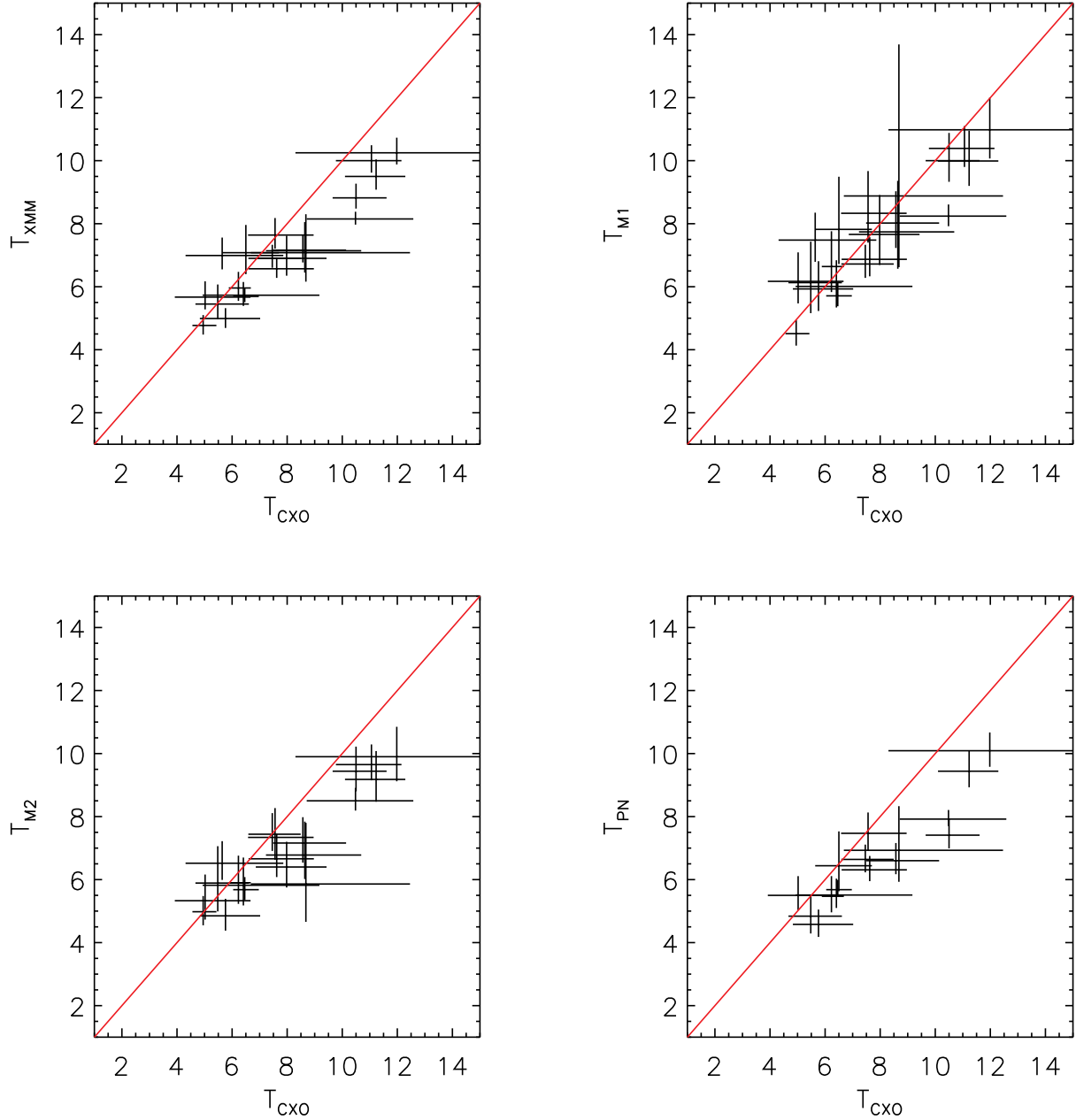


Figure A2. Comparison of the temperatures derived *Chandra* with those derived from the various cameras of *XMM-Newton*. The solid red line is the 1:1 relation. *Top left panel:* Average of temperatures derived from all three *XMM-Newton* cameras versus *Chandra* temperatures. *Top right panel:* *XMM-Newton* MOS1 temperatures versus *Chandra* temperatures. *Bottom left panel:* MOS2 versus *Chandra*. *Bottom right panel:* EPN versus *Chandra*

neers (SPIE) Conference Series, Vol. 5898, Society of Photo-Optical Instrumentation Engineers (SPIE) Conference Series, Siegmund O. H. W., ed., pp. 201–211

Hickox R. C., Markevitch M., 2006, *ApJ*, 645, 95

Jenkins A., Frenk C. S., White S. D. M., Colberg J. M., Cole S., Evrard A. E., Couchman H. M. P., Yoshida N., 2001, *MNRAS*, 321, 372

Kaiser N., 1986, *MNRAS*, 222, 323

Kelly B. C., 2007, *ApJ*, 665, 1489

Kravtsov A. V., Vikhlinin A., Nagai D., 2006, *ApJ*, 650, 128

Kuntz K. D., Snowden S. L., 2000, *ApJ*, 543, 195

Kuntz K. D., Snowden S. L., 2008, *A&A*, 478, 575

Lau E. T., Kravtsov A. V., Nagai D., 2009, *ApJ*, 705, 1129

Leccardi A., Molendi S., 2008, *A&A*, 486, 359

Lumb D. H., Warwick R. S., Page M., De Luca A., 2002, *A&A*, 389, 93

Mahdavi A., Hoekstra H., Babul A., Bildfell C., Jeltrema T., Henry J. P., 2013, *ApJ*, 767, 116

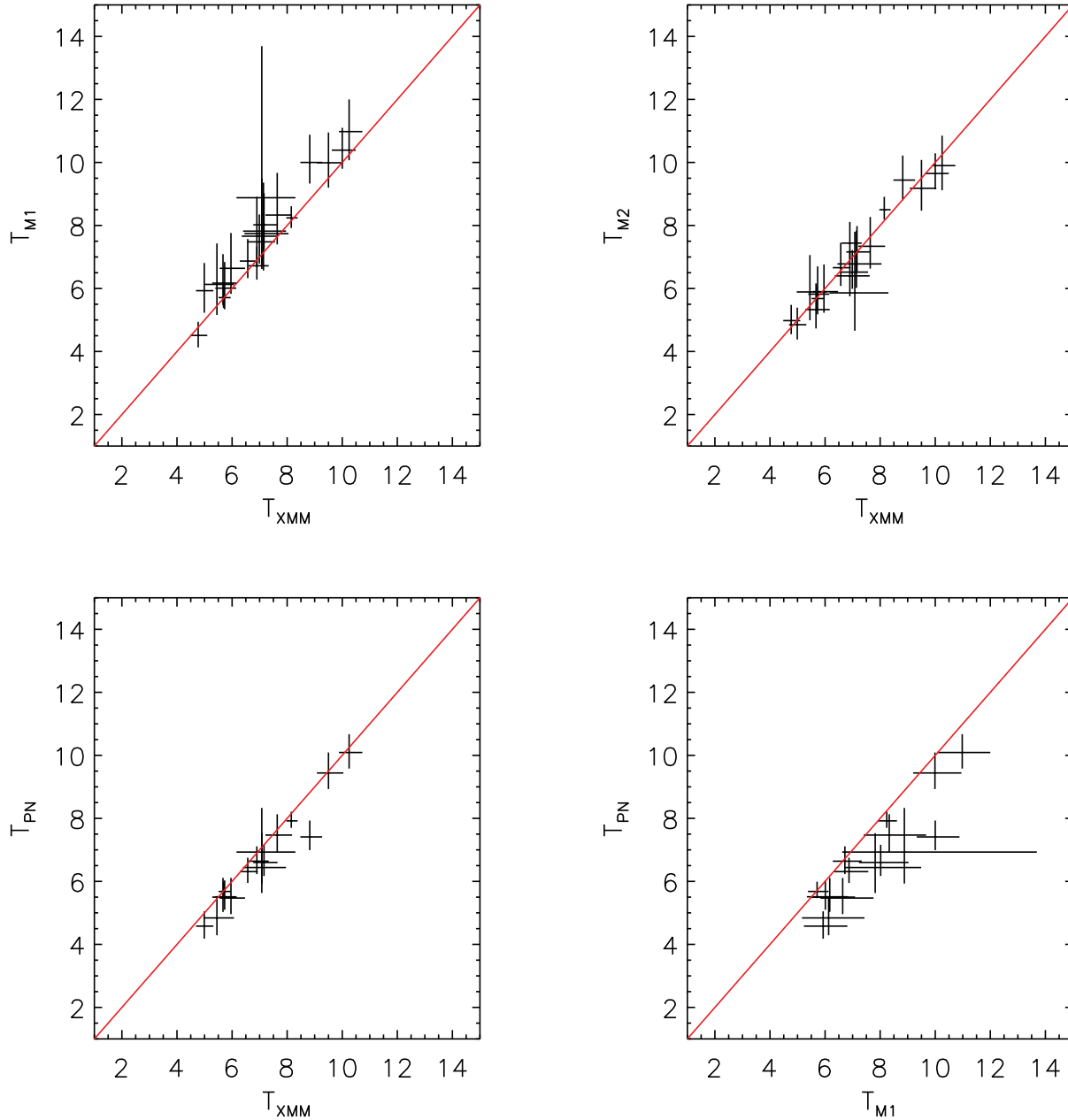


Figure A3. Intercomparison of temperatures derived from the different cameras of *XMM-Newton*. The solid red line is the 1:1 relation. *Top left panel:* *XMM-Newton* MOS1 temperatures versus the temperatures averaged over all three *XMM-Newton* cameras. *Top right panel:* MOS2 versus *XMM-Newton* average. *Bottom left panel:* PN versus *XMM-Newton* average. *Bottom right panel:* PN versus MOS1.

Mahdavi A., Hoekstra H., Babul A., Henry J. P., 2008, *MNRAS*, 384, 1567
Mantz A., Allen S. W., 2011, *ArXiv e-prints*
Markevitch M. et al., 2003, *ApJ*, 583, 70
Marrone D. P. et al., 2012, *ApJ*, 754, 119
Maughan B. J., Jones C., Forman W., Van Speybroeck L., 2008a, *Astrophysical Journals*, 174, 117
Maughan B. J. et al., 2008b, *MNRAS*, 387, 998
Mazzotta P., Rasia E., Moscardini L., Tormen G., 2004, *MNRAS*, 354, 10

Meneghetti M., Rasia E., Merten J., Bellagamba F., Ettori S., Mazzotta P., Dolag K., Marri S., 2010, *A&A*, 514, A93+
Mohr J. J., Evrard A. E., Fabricant D. G., Geller M. J., 1995, *Astrophysical Journal*, 447, 8
Nagai D., 2006, *ApJ*, 650, 538
Nagai D., Vikhlinin A., Kravtsov A. V., 2007, *Astrophysical Journal*, 655, 98
Navarro J. F., Frenk C. S., White S. D. M., 1997, *ApJ*, 490, 493
Neumann D. M., 2005, *A&A*, 439, 465
Nevalainen J., David L., Guainazzi M., 2010, *A&A*, 523, A22

Table A1. Comparison of *Chandra* ACIS-I and *XMM-Newton* temperature estimates

Cluster	$T_{Chandra}$	$T_{XMM,3cameras}$	$T_{XMM,MOS1}$	$T_{XMM,MOS2}$	$T_{XMM,EPN}$
ABELL0115s	$6.46^{+0.51}_{-0.51}$	$5.69^{+0.26}_{-0.26}$	$5.71^{+0.42}_{-0.42}$	$5.68^{+0.40}_{-0.40}$	$5.68^{+0.31}_{-0.31}$
ABELL 1689	$11.23^{+1.06}_{-1.06}$	$9.50^{+0.54}_{-0.54}$	$9.99^{+0.96}_{-0.96}$	$9.18^{+0.90}_{-0.90}$	$9.44^{+0.65}_{-0.65}$
ABELL 1763	$7.98^{+1.45}_{-1.45}$	$6.90^{+0.72}_{-0.72}$	$7.66^{+1.25}_{-1.25}$	$6.40^{+0.80}_{-0.80}$	$0.00^{+0.00}_{-0.00}$
ABELL 1835	$11.06^{+1.09}_{-1.09}$	$10.00^{+0.49}_{-0.49}$	$10.39^{+0.71}_{-0.71}$	$9.65^{+0.64}_{-0.64}$	$0.00^{+0.00}_{-0.00}$
ABELL 1914	$8.57^{+1.57}_{-1.57}$	$7.16^{+0.49}_{-0.49}$	$8.02^{+1.01}_{-1.01}$	$7.16^{+0.82}_{-0.82}$	$6.60^{+0.56}_{-0.56}$
ABELL 0209	$7.56^{+1.40}_{-1.40}$	$7.64^{+0.54}_{-0.54}$	$8.33^{+1.34}_{-1.34}$	$7.34^{+0.93}_{-0.93}$	$7.47^{+0.66}_{-0.66}$
ABELL 2204	$10.50^{+1.11}_{-1.11}$	$8.82^{+0.45}_{-0.45}$	$10.00^{+0.88}_{-0.88}$	$9.44^{+0.78}_{-0.78}$	$7.41^{+0.52}_{-0.52}$
ABELL 2537	$8.68^{+3.78}_{-3.78}$	$7.08^{+1.22}_{-1.22}$	$8.88^{+4.81}_{-4.81}$	$5.86^{+1.94}_{-1.94}$	$6.93^{+1.40}_{-1.40}$
ABELL 2631	$6.50^{+1.20}_{-1.20}$	$7.08^{+0.88}_{-0.88}$	$7.82^{+1.67}_{-1.67}$	$0.00^{+0.00}_{-0.00}$	$6.44^{+1.09}_{-1.09}$
ABELL 2813	$5.48^{+1.13}_{-1.13}$	$5.45^{+0.62}_{-0.62}$	$6.13^{+1.30}_{-1.30}$	$5.89^{+1.17}_{-1.17}$	$4.84^{+0.67}_{-0.67}$
ABELL 0383	$5.76^{+1.26}_{-1.26}$	$4.99^{+0.33}_{-0.33}$	$5.93^{+0.88}_{-0.88}$	$4.85^{+0.54}_{-0.54}$	$4.58^{+0.47}_{-0.47}$
ABELL 0068	$5.02^{+1.65}_{-1.65}$	$5.67^{+0.50}_{-0.50}$	$6.17^{+0.92}_{-0.92}$	$5.33^{+0.83}_{-0.83}$	$5.50^{+0.61}_{-0.61}$
ABELL 0773	$8.64^{+2.05}_{-2.05}$	$7.14^{+0.91}_{-0.91}$	$7.74^{+1.62}_{-1.62}$	$6.78^{+1.06}_{-1.06}$	$0.00^{+0.00}_{-0.00}$
ABELL 0781	$5.64^{+2.22}_{-2.22}$	$6.99^{+0.57}_{-0.57}$	$7.48^{+0.87}_{-0.87}$	$6.52^{+0.70}_{-0.70}$	$0.00^{+0.00}_{-0.00}$
RXC J1504.1–0248	$11.98^{+4.23}_{-4.23}$	$10.25^{+0.48}_{-0.48}$	$10.98^{+1.02}_{-1.02}$	$9.90^{+0.95}_{-0.95}$	$10.09^{+0.58}_{-0.58}$
RX J1720.1+2638	$7.46^{+1.03}_{-1.03}$	$6.90^{+0.43}_{-0.43}$	$6.72^{+0.61}_{-0.61}$	$7.44^{+0.67}_{-0.67}$	$6.64^{+0.47}_{-0.47}$
RX J2129.6+0005	$7.62^{+1.35}_{-1.35}$	$6.57^{+0.36}_{-0.36}$	$6.87^{+0.70}_{-0.70}$	$6.66^{+0.79}_{-0.79}$	$6.31^{+0.44}_{-0.44}$
ZwCl1459.4+4240	$6.41^{+2.76}_{-2.76}$	$5.73^{+0.42}_{-0.42}$	$6.01^{+0.83}_{-0.83}$	$5.82^{+0.88}_{-0.88}$	$5.51^{+0.52}_{-0.52}$
ZwCl 1021.0+0426	$10.48^{+2.10}_{-2.10}$	$8.15^{+0.23}_{-0.23}$	$8.24^{+0.37}_{-0.37}$	$8.50^{+0.41}_{-0.41}$	$7.92^{+0.29}_{-0.29}$
ZwCl 1454.8+2233	$4.95^{+0.48}_{-0.48}$	$4.77^{+0.33}_{-0.33}$	$4.51^{+0.43}_{-0.43}$	$4.98^{+0.50}_{-0.50}$	$0.00^{+0.00}_{-0.00}$
ABELL 0907	$6.23^{+0.45}_{-0.45}$	$5.96^{+0.51}_{-0.51}$	$6.64^{+1.12}_{-1.12}$	$5.90^{+0.86}_{-0.86}$	$5.47^{+0.64}_{-0.64}$

Table A2. Comparison of *Chandra* ACIS-I and *XMM-Newton* temperature estimates

	$T_{XMM,3cameras}$	$T_{XMM,MOS1}$	$T_{XMM,MOS2}$	$T_{XMM,EPN}$
T_{CXO}	0.91 ± 0.03	0.95 ± 0.04	0.90 ± 0.04	0.85 ± 0.03
$T_{XMM,3cameras}$	-	1.04 ± 0.02	1.00 ± 0.02	0.96 ± 0.02
$T_{XMM,MOS2}$	-	1.04 ± 0.03	-	0.94 ± 0.03
$T_{XMM,MOS1}$	-	-	-	0.92 ± 0.03

Okabe N., Smith G. P., Umetsu K., Takada M., Futamase T., 2013, ApJL, 769, L35
 Okabe N., Takada M., Umetsu K., Futamase T., Smith G. P., 2010, PASJ, 62, 811
 Planck Collaboration, 2011, A&A, 536, A11
 Planck Collaboration, 2012, ArXiv e-prints
 Poole G. B., Fardal M. A., Babul A., McCarthy I. G., Quinn T., Wadsley J., 2006, MNRAS, 373, 881
 Popesso P., Biviano A., Böhringer H., Romaniello M., Voges W., 2005, A&A, 433, 431
 Pratt G. W., Böhringer H., Croston J. H., Arnaud M., Borgani S., Finoguenov A., Temple R. F., 2007, A&A, 461, 71
 Pratt G. W., Croston J. H., Arnaud M., Böhringer H., 2009, A&A, 498, 361
 Press W. H., Schechter P., 1974, ApJ, 187, 425
 Press W. H., Teukolsky S. A., Vetterling W. T., Flannery B. P., 1992, Numerical recipes in FORTRAN. The art of scientific computing, Press, W. H., Teukolsky, S. A., Vetterling, W. T., &

Flannery, B. P., ed.
 Rasia E. et al., 2006, MNRAS, 369, 2013
 Rozo E., Rykoff E. S., Bartlett J. G., Evrard A. E., 2012, ArXiv e-prints
 Santos J. S., Tozzi P., Rosati P., Nonino M., Giovannini G., 2012, A&A, 539, A105
 Sarazin C. L., 1988, X-ray Emission from Clusters of Galaxies, Cambridge Astrophysics Series Cambridge: Cambridge University Press., ed.
 Semler D. R. et al., 2012, ApJ, 761, 183
 Sheth R. K., Tormen G., 1999, MNRAS, 308, 119
 Snowden S. L., Mushotzky R. F., Kuntz K. D., Davis D. S., 2008, A&A, 478, 615
 Springel V. et al., 2005, Nature, 435, 629
 Tinker J. L. et al., 2012, ApJ, 745, 16
 Townsley L. K., Broos P. S., Garmire G. P., Nousek J. A., 2000, ApJL, 534, L139
 Tsujimoto M. et al., 2011, A&A, 525, A25

- Vikhlinin A. et al., 2009a, *Astrophysical Journal*, 692, 1033
- Vikhlinin A., Forman W., Jones C., 1999, *Astrophysical Journal*, 525, 47
- Vikhlinin A., Kravtsov A., Forman W., Jones C., Markevitch M., Murray S. S., Van Speybroeck L., 2006, *Astrophysical Journal*, 640, 691
- Vikhlinin A. et al., 2009b, *Astrophysical Journal*, 692, 1060
- Vikhlinin A., Markevitch M., Murray S. S., Jones C., Forman W., Van Speybroeck L., 2005, *Astrophysical Journal*, 628, 655
- Vikhlinin A., McNamara B. R., Forman W., Jones C., Quintana H., Hornstrup A., 1998, *Astrophysical Journal*, 502, 558
- White S. D. M., Navarro J. F., Evrard A. E., Frenk C. S., 1993, *Nature*, 366, 429
- Zhang Y.-Y. et al., 2010, *Astrophysical Journal*, 711, 1033
- Zitrin A. et al., 2012, *MNRAS*, 420, 1621